

Study of the γ -Ray Radiation Properties of High-redshift Blazars at $z > 2.5$

FAN WU ¹ AND BENZHONG DAI ¹

¹*School of Physics and Astronomy, Key Laboratory of Astroparticle Physics of Yunnan Province, Yunnan University, Kunming 650091, P. R. China*

ABSTRACT

We study a sample of 30 high-redshift blazars ($z > 2.5$) by means of spectra and the radiation mechanism with Fermi Large Area Telescope γ -ray observations spanning 15 years. Three models—the power law, power law with an exponential cutoff, and log-parabola—are employed to analyze the spectral properties, and most sources exhibit significant curvature. The high-redshift blazars exhibit higher γ -ray luminosities and softer spectral indices compared with their low-redshift counterparts, where B3 1343+451 has the highest integrated flux, 1.13×10^{-7} ph cm⁻²s⁻¹. We use a standard one-zone leptonic emission model to reproduce the spectral energy distributions of 23 sources with multiwavelength observations. We find that modeling with infrared seed photons is systematically better than with broad-line region (BLR) photons based on a χ^2 test, which suggests that the γ -ray-emitting regions are most likely located outside the BLR. The fit results show that high-redshift blazars exhibit higher energy density, jet power, kinetic power, and accretion disk luminosities, along with lower synchrotron and inverse Compton (IC) peak frequencies, relative to their lower-redshift counterparts. We find that blazars with higher accretion disk luminosities tend to have lower IC peak frequencies, leading to more efficient cooling of high-energy electrons. The positive correlation between jet power and accretion disk luminosity further supports the possibility of an accretion–jet connection in these high-redshift sources.

Keywords: galaxies: active — gamma rays: galaxies — radiation mechanism: non-thermal — galaxies: jets

1. INTRODUCTION

Blazars are a subclass of active galactic nuclei (AGNs). They have a relativistic jet oriented at a small angle with respect to the line of the sight (Urry & Padovani 1995). Based on the absence or presence of broad emission lines, blazars are divided into two subclasses: BL Lacertae objects and flat-spectrum radio quasars (FSRQs) (Stickel et al. 1991). BL Lacertae objects exhibit weak or undetected emission lines, while FSRQs display prominent emission lines.

Blazar spectral energy distributions (SEDs) span from the radio to γ -ray bands, exhibiting a double-peaked structure: a low-energy (LE) peak between infrared (IR) and X-rays, and a high-energy (HE) peak at MeV–TeV γ -rays. The LE component is generally attributed to synchrotron radiation from highly relativistic elec-

trons in the jet (Landau et al. 1986; Ghisellini et al. 1989), while the HE component is thought to result from inverse Compton (IC) scattering, either via synchrotron self-Compton (SSC) (e.g., Bloom & Marscher 1996; Ghisellini et al. 1985) or external Compton (EC) processes. In BL Lacertae objects, SSC dominates the γ -ray emission, whereas EC is more important in FSRQs. The source of external photons is debated, with likely candidates being IR emission from the molecular torus (MT) (e.g., Błażejowski et al. 2000) or optical emission from the broad-line region (BLR) (e.g., Sikora et al. 1994; Ghisellini & Tavecchio 2009; Costamante et al. 2018).

The high-redshift blazars typically show flat or increasing X-ray spectra, especially in the hard X-ray band, have soft γ -ray spectral indices, and possess γ -ray luminosities $> 10^{48}$ ergs s⁻¹. High-redshift blazars are believed to contain supermassive black holes (SMBHs) with masses often $> 10^9 M_{\odot}$ and possess disk luminosi-

ties $> 10^{46}$ ergs s^{-1} (e.g., Ghisellini et al. 2010b; Paliya et al. 2020; Sahakyan et al. 2020; Marcotulli et al. 2020).

High-redshift AGN black holes (BHs) are believed to possess abundant accretable gas, making them more luminous than their low-redshift counterparts (Yuan & Narayan 2004) and able to produce powerful jets (Rees et al. 1982). Their prominent emission lines may originate from various sources, including the jet, hot accretion flows, disk structures, or cold clumps within the hot flow (Sulentic et al. 2000; Taam et al. 2012; Yuan & Narayan 2004; Wielgus et al. 2022; Narayan et al. 2017; Narayan & Raymond 1999; Chiang et al. 2010).

Studying the common properties of high-redshift blazars is important. First, these distant and powerful objects help us understand the physics of relativistic jets and the accretion–jet connection in the early Universe (Ghisellini et al. 2013; Volonteri et al. 2011). Second, they provide valuable constraints on the density of extragalactic background light (EBL) (e.g., Stecker et al. 2007; Franceschini et al. 2008; Finke et al. 2010), which improves our understanding of cosmological evolution (e.g., Ackermann et al. 2012; Fermi-LAT Collaboration et al. 2018; Desai et al. 2019; Finke et al. 2022).

Combining γ -ray data with archival multiwavelength observations helps us to study the physical processes producing their γ -ray emission. It also allows us to understand the properties of relativistic jets in early Universe blazars. This study uses SED theoretical modeling to determine the location of the HE emission region and to understand the radiation properties of the jet. The discussion focuses on the jet dynamics and radiation mechanisms of these high-redshift blazars, and how these findings align with existing radiation models and astrophysical theories.

Given the distant nature of high-redshift blazars, the observational data quality tends to be lower, leading to significant uncertainties in individual SED fitting parameters. However, constructing and analyzing average SEDs from many sources reduces these uncertainties. This approach allows us to compensate for the limitations of individual observations through the power of statistical averaging across larger samples.

The rest of paper is organized as follows. In Section 2, we present the data reduction of the γ -ray observations and describe the SEDs’ observational characteristics. In Section 3, we provide our theoretical modeling of the broadband SEDs and their results. In Section 4, we conduct an in-depth analysis of the possible physical processes that may be responsible for their high-energy emission. Throughout this paper, we adopt a flat cosmological model with $H_0 = 70.5$ km s^{-1} Mpc $^{-1}$, $\Omega_m = 0.27$, and $\Omega_\Lambda = 0.73$.

2. HIGH-ENERGY EMISSION OF HIGH-REDSHIFT BLAZARS

2.1. Sample and Data Reduction

Since 2008, the Fermi Large Area Telescope (Fermi-LAT) has provided a detailed view of the γ -ray sky, capturing images of the entire sky every 3 hr (Atwood et al. 2009). The HE observations are based on the fourth catalog of Fermi-LAT AGNs (4FGL), which contains 3814 blazars, among which 792 are FSRQs, 1458 are BL Lacertae objects, and 1493 are blazar candidates of uncertain type (Abdollahi et al. 2020, 2022). The catalog reports the detection of 110 blazars with redshifts $z > 2$, and only 33 with redshifts $z > 2.5$. We exclude three blazars lacking a confirmed BH mass, synchrotron and IC scattering peak frequency or flux, and accretion disk luminosity. The remaining 30 blazars, which have redshifts $z > 2.5$, were selected as the sample. Detailed information about the sample is presented in Table 1.

The sample data, which span from 2008 August 4 to 2023 November 6 (MJD 54686–60262), were analyzed using Fermi `ScienceTools` version 2.0.8 and the `P8R3_SOURCE_V3` instrument response function. Data were focused on a 15° radius region of interest (ROI) centered on each sample’s γ -ray position, within the 100 MeV–500 GeV energy range. High-probability photon events (`evclass = 128` and `evtype = 3`) were selected with the `gtselect` tool.

A 90° zenith angle cut was applied to minimize contamination from the Earth’s limb. Data were further filtered to include only intervals with good satellite operation and quality, using the `gtmktime` filter expression (`DATA_QUAL>0` && `LAT_CONFIG==1`).

The binned data were prepared using the `gtbin` tool, which allowed for binning the data in the spatial, spectral, and temporal dimensions. A live time cube, which is required for accurate exposure calculations, was created with the `gtlrcube` tool, accounting for variations in the effective area over the entire sky. A likelihood analysis was then performed with the `gtlike` tool to determine the best-fit spectral parameters of each source.

A model file containing spectral parameters was created using the `make4FGLxml.py` script based on the 4FGL catalog, covering the user-defined ROI plus an additional 10 degrees. In the likelihood fit, parameters for sources outside the ROI were fixed, while those within the ROI were allowed to vary. Galactic and extragalactic diffuse γ -ray emissions were modeled using `gll_iem_v07.fits` and `iso_P8R3_SOURCE_V3_v1.txt`, respectively. Note that the data used were not cor-

Table 1. Observations and Environmental Parameters of the Blazar Sample

Fermi name	Source name	R.A.	Dec.	$\log \nu_{\text{syn}}$	$\log \nu F_{\text{syn}}$	$\log \nu_{\text{IC}}$	$\log \nu F_{\text{IC}}$	$\log M_{\text{BH}}$	$\log L_{\text{disk}}$	R_{BLR}	R_{MT}	L_{Edd}	z
				Hz	$\text{erg} \cdot \text{cm}^{-2} \text{s}^{-1}$	Hz	$\text{erg} \cdot \text{cm}^{-2} \text{s}^{-1}$	M_{\odot}	$\text{erg} \cdot \text{s}^{-1}$	$\times 10^{17}$ (cm)	$\times 10^{19}$ (cm)	$\times 10^{47}$ (ergs^{-1})	
J1510.1+5702	GB 1508+5714	227.54	57.04	12.07	-12.21	20.65	-11.72	8.56	46.80	7.94	1.99	0.46	4.314
J1635.6-3628	MG3 J163554+3629	248.92	36.48	13.22	-12.88	21.60	-11.82	9.08	46.25	4.22	1.05	1.51	3.648
J0539.6+1432	TXS 0536+145	84.91	14.54	12.44	-11.94	21.63	-11.33	10.01	46.14	3.72	0.93	12.89	2.710
J0833.4-0458	PMN J0833-0454	128.37	-4.97	12.80	-12.62	21.12	-11.82	9.77	47.17	12.20	3.04	7.42	3.420
J0337.8-1157	PKS 0335-122	54.47	-11.96	12.37	-12.53	21.64	-12.14	8.99	46.21	4.03	1.01	1.23	3.442
J2320.8-0823	PKS 2318-087	350.22	-8.39	12.76	-12.99	20.65	-11.69	9.47	46.48	5.50	1.37	3.72	3.157
J0539.9-2839	PKS 0537-286	84.99	-28.66	11.99	-11.99	20.76	-10.64	10.12	47.04	10.50	2.62	16.61	3.104
J0805.4+6147	TXS 0800+618	121.36	61.79	12.20	-12.24	20.84	-10.80	9.47	46.69	7.00	1.75	3.72	3.033
J1428.9+5406	S4 1427+543	217.23	54.11	12.38	-12.64	21.00	-11.87	9.33	46.19	3.94	0.98	2.69	3.012
J0746.4+2546	B2 0743+25	116.60	25.77	12.26	-12.31	20.45	-10.60	9.37	46.61	6.38	1.60	2.95	2.994
J1344.2-1723	PMN J1344-1723	206.06	-17.40	12.83	-11.53	23.02	-11.20	9.15	46.30	4.47	1.12	1.78	2.516
J1127.4+5648	S4 1124+57	171.86	56.80	12.17	-12.64	20.95	-11.67	8.72	46.80	7.94	1.99	0.66	2.893
J2313.9-4501	PKS 2311-452	348.49	-45.02	12.08	-12.50	20.48	-11.82	8.76	46.25	4.22	1.05	0.73	2.877
J0440.3-4333	PKS 0438-43	70.09	-43.55	11.66	-12.11	20.50	-11.70	9.41	46.59	6.24	1.56	3.24	2.852
J2015.4+6556	S4 2015+65	303.86	65.95	12.59	-12.23	20.75	-11.75	8.82	46.47	5.43	1.36	0.83	2.845
J0836.5-2026	PKS 0834-20	129.13	-20.45	11.90	-11.90	20.85	-10.89	9.48	46.53	5.82	1.46	3.81	2.752
J0224.9+1843	TXS 0222+185	36.23	18.72	12.56	-12.15	20.08	-10.78	9.66	46.73	7.33	1.83	5.76	2.690
J0242.3+1102	OD 166	40.6	11.05	12.45	-11.89	21.18	-11.44	8.81	46.77	7.67	1.92	0.81	2.694
J2339.6+0242	RFC J2338+0251	354.90	2.71	13.09	-12.53	21.38	-11.12	9.05	46.19	3.94	0.98	1.41	2.661
J0910.6+2247	TXS 0907+230	137.67	22.80	12.62	-12.24	21.64	-11.34	8.30	45.93	2.92	0.73	0.25	2.677
J1441.6-1522	PMN J1441-1523	220.41	-15.38	13.00	-12.43	22.28	-11.46	8.39	46.38	4.90	1.22	0.31	2.646
J1054.2+3926	GB6 B1051+3944	163.56	39.43	12.60	-12.98	22.52	-12.38	8.59	45.78	2.45	0.61	0.49	2.635
J1450.4+0910	TXS 1448+093	222.62	9.18	12.97	-12.13	21.60	-11.83	9.15	46.33	4.62	1.16	1.78	2.620
J0226.5+0938	TXS 0223+093	36.63	9.64	13.05	-12.10	22.06	-11.57	10.09	46.61	6.38	1.60	15.50	2.605
J0453.1-2806	PKS 0451-28	73.29	-28.11	12.50	-11.44	20.95	-10.53	9.21	46.88	8.71	2.18	2.04	2.564
J0912.2+4127	B3 0908+416B	138.06	41.46	12.77	-12.23	21.69	-11.58	9.42	45.85	2.66	0.67	3.31	2.568
J1618.0+5139	TXS 1616+517	244.52	51.67	13.60	-12.84	21.27	-11.45	8.78	46.21	4.03	1.01	0.76	2.557
J1625.7+4134	4C+41.32	246.45	41.57	12.03	-12.36	21.21	-11.48	7.85	45.94	2.95	0.74	0.09	2.550
J1345.5+4453	B3 1343+451	206.39	44.88	12.73	-12.59	22.24	-10.84	9.06	46.06	3.39	0.85	1.45	2.542
J2110.2-1021	PKS 2107-105	317.56	-10.36	12.35	-12.27	21.10	-11.54	9.04	46.99	9.89	2.47	1.38	2.500

NOTE—The observations and environmental parameters are presented in columns 5–14, which include the peak frequency and peak flux of synchrotron radiation and IC scattering, BH mass, accretion disk luminosity, radius of the BLR, inner radius of the MT, Eddington luminosity, and redshift, respectively (Chen et al. 2023; Paliya et al. 2021). The BLR and MT are located at distances $R_{\text{BLR}} \simeq 10^{17} \sqrt{L_{\text{disk}}/10^{45} \text{erg s}^{-1}}$ cm and $R_{\text{MT}} \simeq 10^{18} \sqrt{L_{\text{disk}}/10^{45} \text{erg s}^{-1}}$ cm, respectively (Ghisellini & Tavecchio 2008). $L_{\text{Edd}} = \frac{4\pi GMmpc}{\sigma_T} \approx 1.26 \times 10^{38} \left(\frac{M}{M_{\odot}}\right) \text{erg s}^{-1}$.

rected for EBL absorption; observed values postabsorption were employed.

2.2. High-energy Spectral Energy Distributions

Three spectral models were applied to analyze the γ -ray spectral shapes. The first is a simple power law (PL):

$$dN/dE \propto \left(\frac{E}{E_0}\right)^{-\alpha}, \quad (1)$$

where E_0 is the scale energy and α is the PL index.

The second form is a power law with an exponential cutoff (PLC):

$$dN/dE \propto \left(\frac{E}{E_0}\right)^{-\alpha} \exp\left(-\frac{E}{E_c}\right), \quad (2)$$

where E_c is the cutoff energy.

The third form is a log-parabola (LP):

$$dN/dE \propto \left(\frac{E}{E_0}\right)^{-\alpha-\beta \log(E/E_0)}, \quad (3)$$

where β is the curvature index that describes the curvature around the peak. In our analysis, the value of E_0 is set to a fixed value given by FermiTools.

All the best-fitting parameters and spectral normalization factors are presented in Table 2. To evaluate the curvature in the spectra, we computed the test statistic for curvature, $\text{TS}_{\text{curve}} = 2(\log \mathcal{L}_{\text{PLC/LP}} - \log \mathcal{L}_{\text{PL}})$ (Nolan et al. 2012), where $\mathcal{L}_{\text{PLC/LP}}$ and \mathcal{L}_{PL} are the likelihood values estimated for the PLC (or LP) and PL models, respectively. A higher TS_{curve} value indicates a significant deviation from the PL model, favoring models that account for spectral curvature. Table 2 lists the best-fitting model for each source, as determined by the selection criteria outlined above.

The photon indices are generally soft (> 2), with the hardest and softest values being 2.03 ± 0.10 and 2.84 ± 0.13 , respectively. The integrated γ -ray fluxes (above 0.1 GeV) derived from the best-fitting spectral models range from $(0.49\text{--}113.92) \times 10^{-9} \text{ph cm}^{-2} \text{s}^{-1}$. The highest integrated flux is found for B3 1343+451, which has the highest-quality γ -ray data and is one of the most representative known high-redshift blazars (Wu et al.

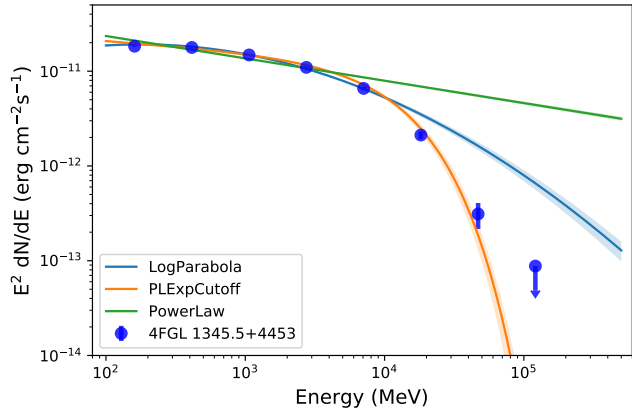


Figure 1. γ -ray spectra of B3 1343+451. The data points are fitted with PL (green), PLC (orange), and LP (blue) models (see text).

2024), its SED is shown in Figure 1, while the other SEDs are provided in Appendix A.

Our results show that the γ -ray spectra of most sources exhibit significant curvature, deviating from the simple PL model. This curvature is well described by the LP and/or PLC models for the majority of the blazars in our sample. The exceptions are PKS 0438-43, TXS 1616+517, and 4C +41.32, whose spectra are adequately fitted by the PL model.

3. BROADBAND SPECTRAL ENERGY DISTRIBUTION MODELING

3.1. Modeling the Broadband Emission

To construct broadband SEDs spanning from the IR to γ -ray bands, we collected multiwavelength data using the Space Science Data Center (SSDC) Sky Explorer.¹ Seven objects were discarded due to a lack of multiwavelength data, and ultimately, we selected 23 blazars with sufficient data coverage for our analysis. Hereafter, physical quantities denoted with a prime (') are measured in the jet's comoving frame, while quantities without a prime are measured in the stationary AGN frame.

We assume that within the jet, there is a plasma blob with radius R' moving along the jet axis with a bulk Lorentz factor Γ . Since the angle between the jet direction and the line of sight to Earth is close to zero, but not exactly zero, we have to consider the Doppler factor, $\delta_D \approx \Gamma$. Inside the blob, there is an anisotropic magnetic field of strength B' . Relativistic electrons, $N'_e(\gamma')$,

are continuously injected, following a specific electron energy distribution (EED). Due to the clear deviation of the γ -ray spectra from a simple PL model, it is likely that the EED has some curvature, which can be modelled with an LP:

$$N'_e(\gamma') = N'_{\text{pk}} \left(\frac{\gamma'}{\gamma'_{\text{pk}}} \right)^{-s-r \log(\gamma'/\gamma'_{\text{pk}})}, \quad (4)$$

where N'_{pk} is the normalization constant at the peak Lorentz factor γ'_{pk} , and s and r are the spectral index and curvature parameter, respectively, which could be indicative of stochastic acceleration of electrons in the jet (e.g., Massaro et al. 2006; Tramacere et al. 2011). To maintain charge neutrality, we assume the presence of protons that are nearly stationary in the comoving frame. These "cold protons" contribute to the kinetic energy of the jet but do not contribute to its nonthermal radiation. The number density of cold protons is assumed to be 0.1 times that of the electrons.

Here, we assume an accretion efficiency of $\eta_{\text{acc}} = 0.3$ for a rapidly rotating BH (Thorne 1974), and the accretion disk is modeled as a geometrically thin, optically thick Shakura–Sunyaev disk (Shakura & Sunyaev 1973; Yuan & Narayan 2014). It extends from the inner radius $R_{\text{in,d}} = 3R_s$ to the outer radius $R_{\text{out,d}} = 10^3 R_s$, where $R_s \equiv 2GM_{\text{BH}}/c^2$ is the Schwarzschild radius and G is the gravitational constant. For additional observational and environmental parameters, see Table 1.

The spectra of the BLR and MT are approximated as isotropic blackbodies peaking at energies corresponding to ~ 10.2 eV and $3.93k_B T_{\text{MT}}$, respectively, where k_B is the Boltzmann constant and T_{MT} is the characteristic temperature of the MT. The BLR photon energy is based on the strong Ly α line commonly observed in blazars. We assume $T_{\text{MT}} = 10^3$ K for the MT radiation. The fractions of accretion disk luminosity reprocessed by the BLR and MT are adopted as $\tau_{\text{BLR}} = 0.1$ and $\tau_{\text{MT}} = 0.2$, respectively.

To determine the appropriate location of the radiation region, we consider potential external photon sources. We assume the dissipation region, R_{diss} , is located near either the BLR or the MT, and we model the emission using the standard one-zone leptonic scenario proposed by Jones (1968); Dermer & Schlickeiser (2002); Tramacere et al. (2011). For high-redshift blazars, the interaction between HE photons and the EBL can be significant. We account for this by converting the intrinsic γ -ray flux to observed flux using the EBL model from Finke et al. (2010).

¹ <http://tools.ssdc.asi.it/SED/>.

Table 2. Three Model Fits for the 30 High-redshift Blazars

Fermi name	$F_{0.1-500\text{GeV}}$	α_{PL}	α_{LP}	α_{PLC}	β	E_{cut}	best model
	$10^{-9} \text{ ph cm}^{-2} \text{ s}^{-1}$	GeV					
J1510.1+5702	5.21 ± 0.81	2.62 ± 0.08	2.48 ± 0.11	2.11 ± 0.31	0.16 ± 0.10	1.65 ± 1.13	LP
J1635.6-3628	8.76 ± 1.84	2.75 ± 0.13	2.75 ± 0.13	2.72 ± 0.17	$(5.37 \pm 5928) \times 10^{-8}$	70.86 ± 24.05	LP
J0539.6+1432	3.26 ± 2.57	–	1.09 ± 0.18	1.16 ± 0.89	0.70 ± 0.10	2.07 ± 1.67	PLC
J0833.4-0458	0.49 ± 0.13	2.04 ± 0.09	1.60 ± 0.29	0.16 ± 0.28	0.88 ± 0.25	1.41 ± 1.29	LP
J0337.8-1157	4.60 ± 0.95	2.54 ± 0.09	2.38 ± 0.16	1.54 ± 0.43	0.44 ± 0.16	0.85 ± 0.45	LP
J2320.8-0823	6.42 ± 1.37	–	1.05 ± 3.06	3.51 ± 0.83	1.90 ± 3.03	226.64 ± 1619.96	PLC
J0539.9-2839	47.62 ± 1.24	2.61 ± 0.02	2.56 ± 0.02	2.35 ± 0.04	0.17 ± 0.02	3.03 ± 0.54	LP
J0805.4+6147	12.53 ± 1.08	2.79 ± 0.06	2.64 ± 0.09	2.49 ± 0.16	0.14 ± 0.06	2.76 ± 1.63	PLC
J1428.9+5406	7.78 ± 1.19	2.75 ± 0.09	2.75 ± 0.11	2.75 ± 0.10	$(7.67 \pm 29082) \times 10^{-9}$	255.33 ± 657.60	PLC
J0746.4+2546	18.25 ± 1.35	2.92 ± 0.06	2.90 ± 0.08	2.52 ± 0.20	0.16 ± 0.08	1.46 ± 0.83	LP
J1344.2-1723	11.87 ± 0.98	2.10 ± 0.02	1.86 ± 0.05	1.73 ± 0.06	0.21 ± 0.03	7.14 ± 1.22	LP
J1127.4+5648	9.16 ± 0.91	2.60 ± 0.06	2.57 ± 0.07	2.51 ± 0.09	0.04 ± 0.04	16.06 ± 14.67	PLC
J2313.9-4501	6.98 ± 1.10	2.84 ± 0.13	2.84 ± 0.14	2.83 ± 0.13	$(5.31 \pm 6431) \times 10^{-8}$	309.92 ± 30.07	LP
J0440.3-4333	71.52 ± 1.48	2.55 ± 0.02	2.63 ± 0.02	2.22 ± 0.04	0.17 ± 0.02	2.63 ± 0.29	PL
J2015.4+6556	0.80 ± 0.23	2.10 ± 0.16	2.23 ± 0.38	–	1.19 ± 0.33	–	LP
J0836.5-2026	8.24 ± 1.47	2.81 ± 0.10	2.43 ± 0.21	1.72 ± 0.55	0.47 ± 0.22	0.53 ± 0.32	PLC
J0224.9+1843	2.86 ± 1.00	–	1.79 ± 0.36	1.60 ± 1.01	0.56 ± 0.29	0.94 ± 1.47	LP
J0242.3+1102	11.55 ± 1.30	2.45 ± 0.04	2.24 ± 0.08	1.65 ± 0.18	0.39 ± 0.07	1.30 ± 0.36	LP
J2339.6+0242	0.79 ± 0.18	2.09 ± 0.10	1.08 ± 0.28	–	0.87 ± 0.18	0.97 ± 0.40	LP
J0910.6+2247	5.69 ± 1.13	2.32 ± 0.07	2.22 ± 0.10	2.08 ± 0.14	0.10 ± 0.06	11.89 ± 6.99	PLC
J1441.6-1522	0.83 ± 0.33	2.03 ± 0.10	1.85 ± 0.21	1.34 ± 0.40	0.35 ± 0.13	5.54 ± 3.42	LP
J1054.2+3926	0.90 ± 0.44	2.10 ± 0.16	1.83 ± 3.38	0.75 ± 0.45	0.66 ± 1.68	1.94 ± 2.86	LP
J1450.4+0910	2.72 ± 0.49	2.19 ± 0.05	1.79 ± 0.12	1.45 ± 0.18	0.41 ± 0.08	3.02 ± 0.85	LP
J0226.5+0938	1.56 ± 0.81	2.12 ± 0.10	2.03 ± 0.17	1.87 ± 0.21	0.14 ± 0.09	21.70 ± 19.37	LP
J0453.1-2806	53.06 ± 1.26	2.60 ± 0.02	2.44 ± 0.03	2.37 ± 0.04	0.13 ± 0.02	3.76 ± 0.66	PLC
J0912.2+4127	15.76 ± 1.06	2.48 ± 0.04	2.47 ± 0.04	2.40 ± 0.06	0.07 ± 0.03	19.53 ± 13.20	PLC
J1618.0+5139	0.51 ± 0.16	2.43 ± 0.15	0.53 ± 0.32	–	1.14 ± 0.28	0.68 ± 0.31	PL
J1625.7+4134	8.03 ± 0.79	2.39 ± 0.05	1.82 ± 0.13	1.49 ± 0.21	0.44 ± 0.09	1.81 ± 0.55	PL
J1345.5+4453	113.92 ± 1.15	2.24 ± 0.01	2.16 ± 0.01	2.11 ± 0.01	0.08 ± 0.01	11.55 ± 1.01	PLC
J2110.2-1021	3.41 ± 1.28	2.52 ± 0.18	1.87 ± 0.40	2.51 ± 0.21	0.63 ± 0.38	195.78 ± 955.92	PLC

NOTE—Column 2 is the γ -ray flux from the best-fit model. Columns 3–7 are the fitting parameters for each of the three models. Column 8 is the best-fit model for the observation period. Models that cannot be fitted are represented by “–.” When the error of the fitted value is greater than the magnitude of the original data, it is considered an inaccurate parameter and is marked in **bold**.

Table 3. Parameters Obtained from the Modeling

R _{diss}	Fermi name	N' _{pk}		s	r	δD	γ _{pk}	B'	R'	P _e		P _p		P _r		P _{jet}	CD	χ ² /χ _{dof} ²
		×10 ³	(1/cm ³)							×10 ¹⁵	×10 ¹⁴	×10 ¹⁵	×10 ¹⁴	×10 ¹⁵	×10 ¹⁴			
R _{diss} = R _{BLR}	J1510.1+5702	10.33 ^{+1.16} _{-1.39}	7.53 ^{+0.74} _{-0.53}	1.99 ^{+0.25} _{-0.17}	15.03 ^{+0.80} _{-0.68}	9.38 ^{+1.32} _{-1.25}	2.04 ^{+0.20} _{-0.19}	4.15 ^{+0.40} _{-0.35}	8.72	0.60	1.55	5.64	3.05	14.45	2.95/12.73			
	J1635.6+3628	1.81 ^{+0.24} _{-0.24}	8.40 ^{+0.44} _{-0.44}	1.34 ^{+0.10} _{-0.10}	10.60 ^{+0.55} _{-0.55}	103.21 ^{+14.33} _{-14.33}	1.85 ^{+0.17} _{-0.17}	9.97 ^{+1.07} _{-1.07}	4.22	1.43	1.74	2.85	2.59	2.96	7.41/4.75			
	J0539.6+1432	428.77 ^{+63.07} _{-51.22}	2.77 ^{+0.14} _{-0.14}	1.14 ^{+0.04} _{-0.04}	26.09 ^{+1.24} _{-1.15}	0.16 ^{+0.01} _{-0.01}	4.79 ^{+0.26} _{-0.26}	1.32 ^{+0.13} _{-0.13}	16.90	1.01	1.72	71.50	10.70	16.74	159.2/6.80			
	J0359.9+2839	533.41 ^{+50.21} _{-49.78}	7.45 ^{+0.29} _{-0.34}	1.44 ^{+0.07} _{-0.07}	5.37 ^{+0.24} _{-0.24}	101.02 ^{+12.07} _{-11.32}	2.48 ^{+0.26} _{-0.31}	1.13 ^{+0.07} _{-0.07}	12.80	0.008	1.50	2.73	151	1534.48	8.06/7.89			
	J0805.4+6147	21.81 ^{+2.86} _{-2.86}	7.68 ^{+0.89} _{-0.89}	6.11 ^{+0.53} _{-0.53}	8.54 ^{+0.39} _{-0.39}	2.63 ^{+0.37} _{-0.37}	1.79 ^{+0.11} _{-0.11}	3.61 ^{+0.31} _{-0.31}	12.80	0.11	10.10	2.91	11.70	112.80	9.21/3.75			
	J1428.9+5406	80.28 ^{+8.15} _{-8.15}	1.49 ^{+0.13} _{-0.13}	1.24 ^{+0.09} _{-0.09}	10.10 ^{+0.63} _{-0.63}	0.51 ^{+0.06} _{-0.06}	3.28 ^{+0.25} _{-0.25}	1.14 ^{+0.09} _{-0.09}	4.19	0.05	3.92	1.50	4.50	78.75	2.67/3.79			
	J0746.4+2546	2.68 ^{+0.33} _{-0.33}	6.16 ^{+0.35} _{-0.35}	0.69 ^{+0.05} _{-0.05}	31.80 ^{+1.39} _{-1.39}	4.40 ^{+0.72} _{-0.72}	6.24 ^{+0.88} _{-0.88}	34.3 ^{+2.39} _{-2.39}	9.06	1740.00	3.51	451	223	0.0052	9.98/29.31			
	J1344.2-1723	24.70 ^{+4.52} _{-4.52}	8.70 ^{+1.63} _{-1.63}	1.92 ^{+0.25} _{-0.25}	45.01 ^{+3.45} _{-3.45}	24.50 ^{+5.94} _{-5.94}	8.01 ^{+0.94} _{-0.94}	0.29 ^{+0.03} _{-0.03}	1.06	0.41	0.11	0.60	0.31	2.56	15.28/26.38			
	J1227.4+5648	282.03 ^{+46.81} _{-46.81}	3.48 ^{+0.17} _{-0.17}	0.18 ^{+0.03} _{-0.03}	6.93 ^{+0.48} _{-0.48}	127.75 ^{+24.02} _{-23.30}	0.70 ^{+0.05} _{-0.05}	24.81 ^{+3.49} _{-3.44}	41.60	0.53	5.02	1170.00	126.00	78.64	1.21/4.86			
	J0440.3-4333	1.60 ^{+0.18} _{-0.18}	2.20 ^{+0.07} _{-0.07}	0.55 ^{+0.02} _{-0.02}	7.22 ^{+0.24} _{-0.24}	0.33 ^{+0.03} _{-0.03}	0.80 ^{+0.03} _{-0.03}	67.03 ^{+5.44} _{-5.44}	21.80	5.61	25.00	52.50	33.00	3.88	0.1/4.81			
	J2015.4+6556	0.87 ^{+0.11} _{-0.11}	3.16 ^{+0.10} _{-0.10}	0.78 ^{+0.03} _{-0.03}	7.83 ^{+0.40} _{-0.39}	0.39 ^{+0.04} _{-0.04}	2.08 ^{+0.14} _{-0.14}	110.12 ^{+10.62} _{-9.22}	16.50	119	12.90	90.40	35.50	0.14	1.37/3.68			
	J0836.5+2026	21.50 ^{+1.93} _{-1.93}	4.68 ^{+0.19} _{-0.19}	1.41 ^{+0.08} _{-0.08}	6.71 ^{+0.43} _{-0.43}	7.04 ^{+0.86} _{-0.86}	3.94 ^{+0.26} _{-0.26}	3.63 ^{+0.26} _{-0.26}	5.06	0.34	1.79	15.50	16.20	14.83	5.91/8.32			
	J0224.9+1843	2.92 ^{+0.48} _{-0.48}	4.50 ^{+0.20} _{-0.20}	0.29 ^{+0.03} _{-0.03}	23.50 ^{+0.61} _{-0.61}	5.44 ^{+1.09} _{-1.09}	9.24 ^{+1.11} _{-1.11}	75.02 ^{+5.97} _{-5.12}	11.70	9930	2.44	1110	1110	0.0012	0.49/7.47			
	J2339.6+0242	0.0053 ^{+0.001} _{-0.001}	8.70 ^{+0.85} _{-0.85}	3.03 ^{+0.35} _{-0.35}	78.60 ^{+6.67} _{-6.67}	104.02 ^{+23.70} _{-23.44}	8.21 ^{+0.33} _{-0.33}	1.31 ^{+0.22} _{-0.22}	1.57	227.00	0.004	0.008	2.68	0.00027	1.95/15.46			
	J0910.6+2247	3.03 ^{+0.30} _{-0.30}	7.95 ^{+0.38} _{-0.38}	3.15 ^{+0.05} _{-0.05}	11.02 ^{+0.50} _{-0.50}	7.29 ^{+0.74} _{-0.74}	2.02 ^{+0.14} _{-0.14}	4.26 ^{+0.31} _{-0.31}	3.48	0.33	0.94	0.94	1.45	10.42	15.19/12.57			
	J1054.2+3926	19.80 ^{+3.04} _{-2.87}	8.27 ^{+0.53} _{-0.47}	1.72 ^{+0.15} _{-0.15}	11.20 ^{+0.81} _{-0.81}	30.40 ^{+3.89} _{-3.89}	2.66 ^{+0.27} _{-0.27}	2.46 ^{+0.27} _{-0.27}	3.74	0.20	0.71	2.12	1.32	18.68	2.64/3.24			
	J0226.5+0938	0.0036 ^{+0.0006} _{-0.0006}	7.75 ^{+0.69} _{-0.69}	3.03 ^{+0.35} _{-0.35}	5.55 ^{+0.40} _{-0.40}	4.79 ^{+0.85} _{-0.85}	2.17 ^{+0.26} _{-0.26}	206.43 ^{+29.03} _{-29.03}	1.57	227.00	0.66	0.66	30.50	0.0069	15.65/18.27			
	J0453.1-2806	11.60 ^{+0.98} _{-0.98}	6.11 ^{+0.25} _{-0.25}	1.00 ^{+0.06} _{-0.06}	10.90 ^{+0.44} _{-0.44}	56.80 ^{+5.79} _{-5.79}	2.83 ^{+0.38} _{-0.38}	6.32 ^{+0.38} _{-0.38}	11.60	1.42	7.76	11.10	13.20	8.19	3.01/7.79			
	J0912.2+4127	2.39 ^{+0.37} _{-0.37}	4.86 ^{+0.12} _{-0.12}	0.41 ^{+0.02} _{-0.02}	20.40 ^{+1.29} _{-1.13}	40.60 ^{+5.15} _{-4.20}	3.73 ^{+0.25} _{-0.25}	23.4 ^{+1.96} _{-1.90}	2.70	119.00	1.14	77.00	21.00	0.023	9.11/4.18			
	J1618.0+5139	9.35 ^{+1.26} _{-1.26}	7.28 ^{+0.32} _{-0.32}	1.30 ^{+0.09} _{-0.09}	11.50 ^{+0.66} _{-0.66}	55.40 ^{+6.56} _{-6.56}	2.30 ^{+0.15} _{-0.15}	2.94 ^{+0.25} _{-0.25}	2.74	0.23	0.53	1.51	0.97	11.96	0.2/4.98			
J1625.7+4134	298.45 ^{+66.31} _{-55.13}	7.03 ^{+1.04} _{-0.78}	4.54 ^{+0.46} _{-0.46}	32.60 ^{+3.07} _{-2.44}	1.45 ^{+0.21} _{-0.21}	3.09 ^{+0.35} _{-0.35}	0.20 ^{+0.02} _{-0.02}	3.40	0.02	0.77	1.77	0.59	225.07	5.49/3.69				
J1345.5+4453	23.50 ^{+2.37} _{-2.50}	8.02 ^{+0.24} _{-0.24}	1.50 ^{+0.07} _{-0.07}	36.40 ^{+2.64} _{-3.17}	38.01 ^{+3.43} _{-3.43}	1.49 ^{+0.11} _{-0.11}	0.88 ^{+0.06} _{-0.06}	4.74	0.09	0.76	3.44	1.58	55.07	23.27/10.98				
Average	7.75 × 10 ⁴	6.04	1.65	18.87	3.29 × 10 ⁴	3.51	2.55 × 10 ¹⁶	8.75 × 10 ¹⁶	5.29 × 10 ¹⁶	1.33 × 10 ¹⁶	1.12 × 10 ¹⁶	7.82 × 10 ¹⁶	7.82 × 10 ¹⁶	1.58	23.27/10.98			
R _{diss} = R _M	J1510.1+5702	0.11 ^{+0.03} _{-0.03}	1.54 ^{+0.12} _{-0.12}	0.42 ^{+0.04} _{-0.04}	40.40 ^{+2.82} _{-2.82}	3.03 ^{+0.76} _{-0.63}	0.20 ^{+0.02} _{-0.02}	28.30 ^{+3.51} _{-3.51}	6.91	203.79	5.09	20.91	23.69	0.34	1.86/14.94			
	J1635.6+3628	1.06 ^{+0.16} _{-0.16}	1.06 ^{+0.13} _{-0.13}	0.60 ^{+0.03} _{-0.03}	31.50 ^{+2.41} _{-2.41}	9.67 ^{+1.28} _{-1.28}	0.18 ^{+0.02} _{-0.02}	7.61 ^{+0.84} _{-0.84}	11.12	6.59	4.56	8.62	9.84	16.87	2.31/4.92			
	J0539.6+1432	0.09 ^{+0.01} _{-0.01}	1.89 ^{+0.07} _{-0.07}	0.46 ^{+0.02} _{-0.02}	37.30 ^{+2.52} _{-1.88}	6.54 ^{+0.90} _{-0.88}	0.31 ^{+0.02} _{-0.02}	0.18 ^{+0.02} _{-0.02}	9.26	870.94	6.95	31.50	41.21	0.11	13.07/6.44			
	J0359.9+2839	1.35 ^{+0.18} _{-0.18}	1.12 ^{+0.10} _{-0.10}	0.75 ^{+0.02} _{-0.02}	41.10 ^{+1.55} _{-1.55}	7.87 ^{+1.19} _{-1.19}	0.11 ^{+0.007} _{-0.007}	14.9 ^{+1.03} _{-1.03}	58.25	18.26	31.92	77.66	77.99	31.90	5.62/7.34			
	J0805.4+6147	0.017 ^{+0.002} _{-0.002}	1.82 ^{+0.09} _{-0.09}	0.70 ^{+0.03} _{-0.03}	75.80 ^{+2.91} _{-2.91}	7.69 ^{+1.15} _{-1.15}	0.56 ^{+0.04} _{-0.04}	25.62 ^{+2.32} _{-2.32}	2.94	4408.95	3.53	8.80	53.21	0.0067	7.75/4.09			
	J1428.9+5406	16.22 ^{+1.44} _{-1.44}	2.67 ^{+0.11} _{-0.11}	1.06 ^{+0.07} _{-0.07}	55.60 ^{+0.37} _{-0.37}	2042.01 ^{+238.32} _{-237.19}	2.83 ^{+0.27} _{-0.27}	0.43 ^{+0.03} _{-0.03}	0.39	0.17	131.25	0.013	1.37	23.65	2.21/3.78			
	J0746.4+2546	0.0015 ^{+0.0002} _{-0.0002}	1.32 ^{+0.09} _{-0.09}	0.89 ^{+0.02} _{-0.02}	72.30 ^{+2.50} _{-2.50}	5.87 ^{+0.62} _{-0.62}	0.42 ^{+0.02} _{-0.02}	65.13 ^{+4.45} _{-4.45}	2.11	14296.31	7.02	4.70	147.95	0.0015	2.88/27.80			
	J1344.2-1723	2.37 ^{+0.49} _{-0.49}	1.36 ^{+0.23} _{-0.23}	1.70 ^{+0.20} _{-0.20}	103.03 ^{+8.63} _{-8.77}	313.01 ^{+74.44} _{-56.31}	0.75 ^{+0.10} _{-0.10}	0.12 ^{+0.02} _{-0.02}	0.88	0.29	0.050	0.25	0.14	29.73	12.61/16.07			
	J1127.4+5648	10123 ^{+1854.22} _{-1711.09}	4.23 ^{+0.39} _{-0.39}	0.46 ^{+0.08} _{-0.08}	85.80 ^{+6.42} _{-5.92}	3101.77 ^{+644.21} _{-576.89}	0.33 ^{+0.03} _{-0.03}	0.10 ^{+0.01} _{-0.01}	38.21	0.03	109.52	0.42	113.34	12528.67	0.61/5.31			
	J2313.9-4501	5.50 ^{+0.81} _{-0.81}	2.44 ^{+0.09} _{-0.09}	0.51 ^{+0.05} _{-0.05}	30.40 ^{+2.22} _{-2.22}	2760.21 ^{+413.41} _{-413.41}	1.24 ^{+0.13} _{-0.13}	1.24 ^{+0.13} _{-0.13}	0.25	0.10	1.07	0.014	1.07	0.05	24.11	1.76/3.27		
	J0440.3-4333	0.39 ^{+0.04} _{-0.04}	4.43 ^{+0.14} _{-0.14}	1.14 ^{+0.05} _{-0.05}	6.82 ^{+0.29} _{-0.29}	27917.36 ^{+3041.78} _{-3041.78}	0.19 ^{+0.01} _{-0.01}	5.45 ^{+0.33} _{-0.33}	5.86	0.18	0.075	0.075	5.21	334.16	2.55/5.62			
	J2015.4+6556	0.44 ^{+0.07} _{-0.07}	1.55 ^{+0.08} _{-0.08}	0.48 ^{+0.02} _{-0.02}	49.40 ^{+2.74} _{-2.74}	3.14 ^{+0.33} _{-0.33}	0.51 ^{+0.04} _{-0.04}	10.90 ^{+0.10} _{-0.10}	5.52	283.66	18.11	2.05	21.51	0.19	0.12/2.58			
	J0836.5+2026	89.10 ^{+8.55} _{-8.55}	2.10 ^{+0.14} _{-0.14}	1.28 ^{+0.08} _{-0.08}	29.50 ^{+1.82} _{-1.82}	788.09 ^{+91.23} _{-91.23}	0.84 ^{+0.07} _{-0.07}	0.093 ^{+0.007} _{-0.007}	2.36	0.02	6.95	0.095	0.40	1172.97	4.16/8.36			
	J0224.9+1843	3.92 ^{+0.46} _{-0.46}	5.15 ^{+0.23} _{-0.23}	1.40 ^{+0.07} _{-0.07}	9.70 ^{+0.38} _{-0.38}	13404.97 ^{+1881.05} _{-1533.78}	0.17 ^{+0.01} _{-0.01}	2.79 ^{+0.20} _{-0.20}	14.55	0.076	0.40	170.92	3.57	1910.79	1.03/7.98			
	J2339.6+0242	0.27 ^{+0.09} _{-0.09}	1.57 ^{+0.39} _{-0.39}	0.31 ^{+0.16} _{-0.16}	42.30 ^{+5.03} _{-5.03}	3.34 ^{+1.17} _{-1.17}	0.22 ^{+0.03} _{-0.03}	5.53 ^{+1.47} _{-1.47}	0.86	9.83	0.30	2.11	2.29	0.87	4.98/15.66			
	J0910.6+2247	3.43 ^{+0.37} _{-0.37}	2.82 ^{+0.32} _{-0.32}	2.89 ^{+0.07} _{-0.07}	36.51 ^{+2.11} _{-2.11}	1750.39 ^{+194.24} _{-170.39}	0.23 ^{+0.02} _{-0.02}	0.28 ^{+0.02} _{-0.02}	2.86	0.02	1.39	0.05	0.35	1425.59	6.19/12.29			
	J1054.2+3926																	

Table 4. Normality Test Results (Shapiro–Wilk)

Parameter	Shapiro–Wilk Statistic	p -value
B'	0.9527	0.3328
$\log P_e$	0.9771	0.8518
$\log P_B$	0.9368	0.1530
$\log P_r$	0.9153	0.0530
$\log P_{\text{jet}}$	0.9702	0.6935
$\log \nu_{\text{syn}}$	0.9786	0.8817
$\log \nu_{\text{IC}}$	0.9494	0.2843
$\log M_{\text{BH}}$	0.9759	0.8265
$\log L_{\text{disk}}$	0.9649	0.5695

NOTE—A Shapiro–Wilk statistic close to 1 and $p > 0.05$ indicates that the parameter set follows a normal distribution.

3.2. Spectral Energy Distribution Modeling Results

We fit the SEDs over the energy range from IR to γ -rays (10^{12} – 10^{28} Hz). The LE peak is assumed to be dominated by synchrotron radiation, while the HE peak is primarily due to IC scattering. The seed photons for IC scattering originate from two sources: (1) reprocessed emission from the BLR in the optical–UV range, and (2) reprocessed IR emission from the MT (Sikora et al. 2009). The radio band, which is thought to originate from a larger region outside the jet, is excluded from the fit. Since our study focuses on high-redshift blazars, we also account for the effects of EBL absorption.

The dissipation region, R_{diss} , is constrained to be near either R_{BLR} or R_{MT} . Seven free parameters are included in the fit: N'_{pk} , s , r , δ_{D} , γ'_{pk} , B' , and R' . The SEDs are derived from theoretical modeling, calculated using the publicly available `JetSet` package (Massaro et al. 2006; Tramacere et al. 2009, 2011). We consider data above 10^{12} Hz, and the model is optimized using the `emcee` optimizer (Foreman-Mackey et al. 2013).

We collect the peak frequency and peak flux of the synchrotron and IC bumps from Abdollahi et al. (2022); Chen et al. (2023), while the BH masses and disk luminosities are taken from Xiao et al. (2022). Based on the environmental parameters listed in Table 1, we obtained the model parameters, power parameters, and fit curves for the 23 blazars with good data coverage. The best-fit values and their 1σ errors are summarized in Table 3. As an example, the typical SED of B3 1343+451 is shown in Figure 2, while the complete fitting results are

provided in Appendix B. Our results represent the general state during the period of observation. It can be observed that for blazars with redshift > 2.5 , the effect of EBL absorption only becomes significant at energy levels $> 10^{25}$ Hz.

In the BLR case, the X-ray emission is mostly attributed to the SSC process, except for sources B2 0743+25, TXS 0222+185, and B3 0908+416B. In the MT case, the X-ray band is dominated by either SSC or EC processes. Table 3 lists the chi-square values for the γ -ray band fits. The lower chi-square values for the MT scenario compared to the BLR suggest that the radiation region is more likely located near the MT, where seed photons are provided by IR photons, consistent with previous studies of high-redshift blazars (Sahakyan et al. 2020; Wu et al. 2024).

Following Celotti & Ghisellini (2008), we evaluated the power carried by the magnetic field (P_B), emitting electrons/positrons (P_e), radiation (P_r), and cold protons (P_p) in the jet. The cold proton number density is assumed to be 10% of the electron number density.

No matter where the radiation region is, we find that the jet kinetic power $P_{\text{kin}} = P_e + P_B + P_p$ is higher than P_r or L_{disk} , ensuring the continuous and stable ejection of jet. This is consistent with the conclusions of Paliya et al. (2017); Ghisellini et al. (2014); Chen et al. (2023). We also find that P_e is lower than P_B , which is likely due to high-redshift blazars exist in a photon-rich environment, allowing the electrons within the blob to cool more efficiently via the IC process (Fan et al. 2023).

The Compton dominance (CD) is used to characterize the proportion of IC scattering relative to synchrotron radiation. As shown in Table 3, we find that for high-redshift blazars, it is challenging to distinguish between particle-dominated or Poynting flux-dominated jets directly solely through parameter fitting, consistent with the conclusions of Fan et al. (2023). While equipartition might exist between the magnetic field and non-thermal electron energy density, this balance is disrupted when considering the protons in the jet, whose content/proportion remains uncertain (Sahakyan 2020). Future observations, particularly those investigating polarization properties and variability timescales, could provide additional constraints on the jet content and structure.

3.3. Correlation among the Parameters

We used kernel density estimation to determine the probability density function of each parameter, as shown in Figure 3. The figure indicates that the parameters cover similar ranges across the sample. To evaluate the parameter distributions further, we applied the Shapiro–

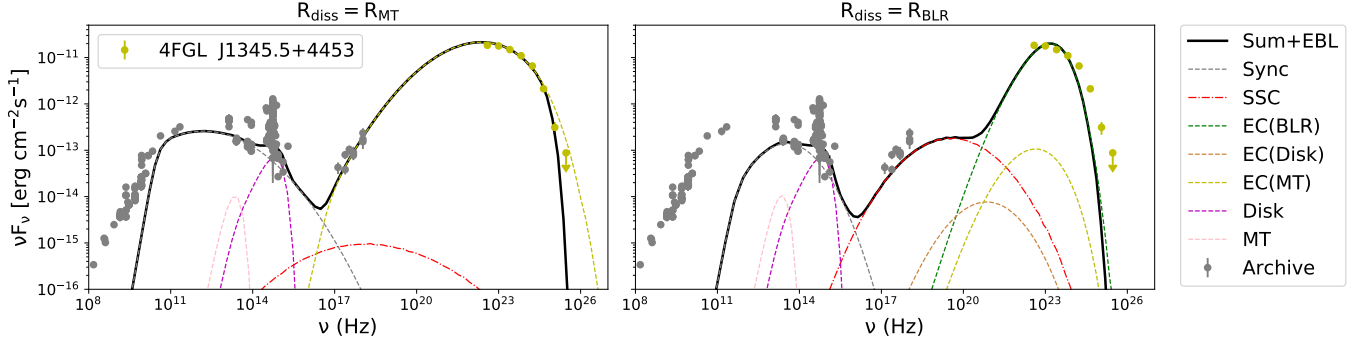


Figure 2. The left and right panels represent the best fits with $R_{\text{diss}} = R_{\text{MT}}$ and $R_{\text{diss}} = R_{\text{BLR}}$, respectively. The grey points from the radio to X-ray bands represent the historical data obtained from the SSDC Sky Explorer. Separate synchrotron, MT, accretion disk, SSC, EC-disk, EC-BLR, and EC-MT components are shown. The black solid line in all plots represents the sum of all components, which have been corrected for EBL absorption considering the model of Finke et al. (2010)

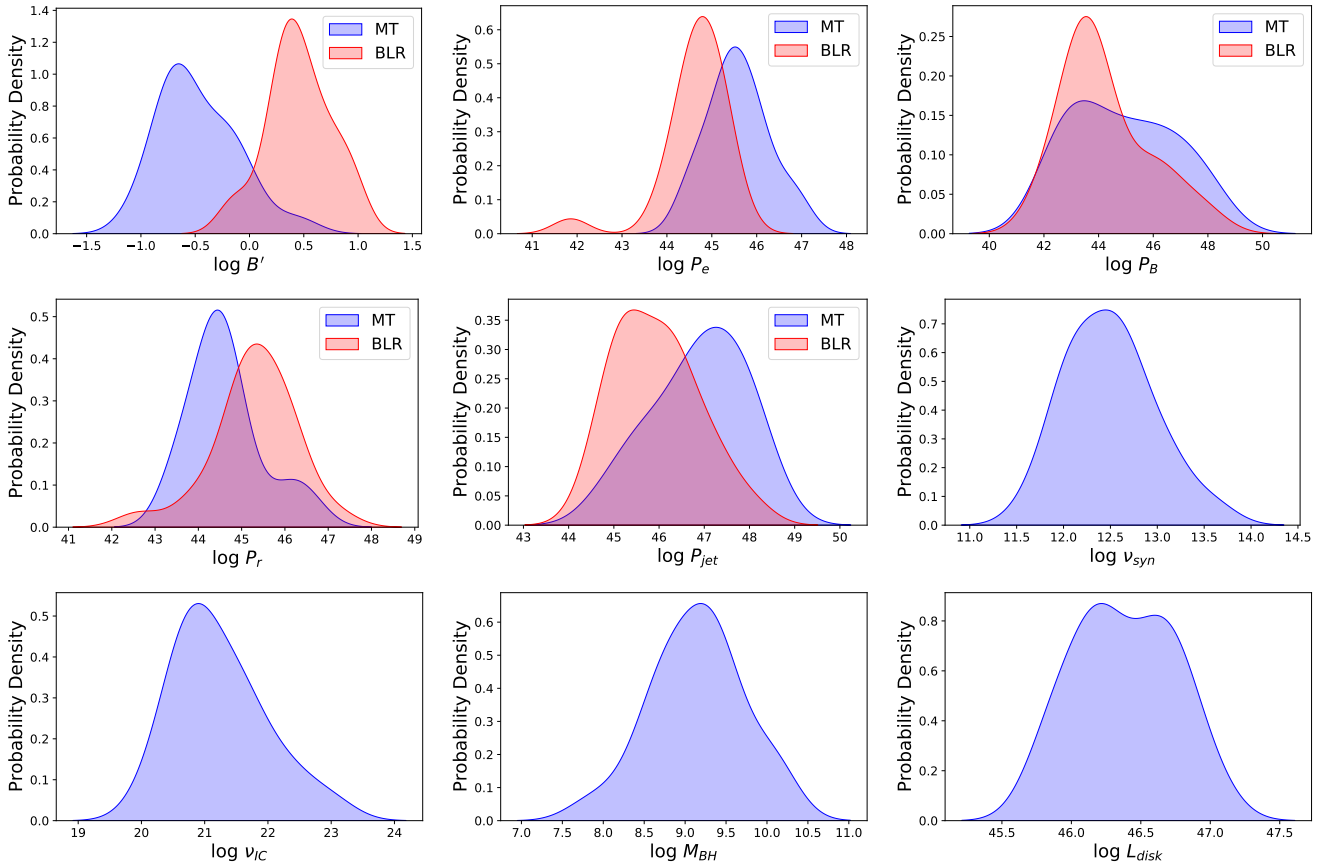


Figure 3. The distributions of the physical parameters. The red line is $R_{\text{diss}} = R_{\text{BLR}}$ and the blue line is $R_{\text{diss}} = R_{\text{MT}}$.

Wilk normality test. The corresponding Shapiro–Wilk statistics and chance probability (i.e., p -values) are presented in Table 4, which confirm that all of the parameters in the table follow a normal distribution.

Understanding correlations between parameters is crucial for interpreting the physical processes in blazars. Above, we found that these parameters all passed the

normality test. Next, we proceeded to compute the Pearson correlation coefficient ² (r) to analyze potentially correlated parameter pairs. Figures 4 and 5

² When using the Pearson correlation coefficient to measure a linear relationship between two variables, it is recommended that the variables approximately follow a normal distribution.

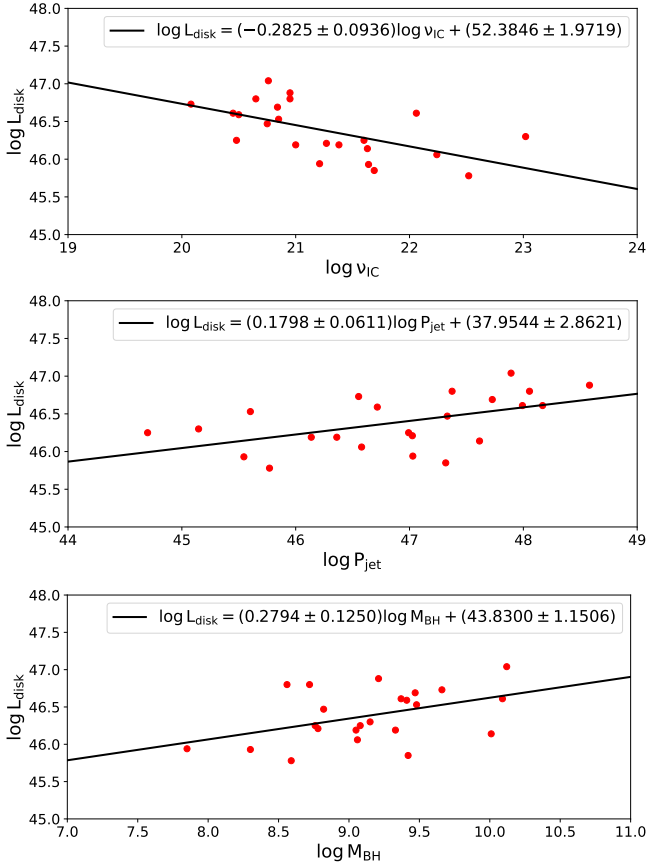


Figure 4. Linear relationships between the accretion disk luminosity and IC peak frequency ($r = -0.5774$, $p = 0.0039$), jet power ($r = 0.5245$, $p = 0.0102$), and BH mass ($r = 0.4418$, $p = 0.0348$) are shown.

present the correlation fitting curves among selected parameters, which quantify the strength of their linear relationships and the statistical significance of the results.

The correlation coefficients of the parameter pairs are between 0.4 and 0.7, indicating moderate correlation—there is a clear relationship between the variables, but the data points show considerable scatter, and the chance probability is $p < 0.05$ —meaning the empirical relations can be obtained by linear regression analysis.

4. DISCUSSION AND CONCLUSION

4.1. High-energy Radiation Properties

The γ -ray fluxes we obtained range from $(0.49\text{--}113.92) \times 10^{-9}$ ph cm $^{-2}$ s $^{-1}$, which is comparable to that of their low-redshift counterparts (Zhu et al. 2024). The fact that such distant blazars can still receive such high fluxes may be that early AGNs have a higher external photon field density, which leads to increased IC scattered luminosities. Additionally, selection effects can also provide an explanation, as high-redshift AGNs must be powerful enough to be de-

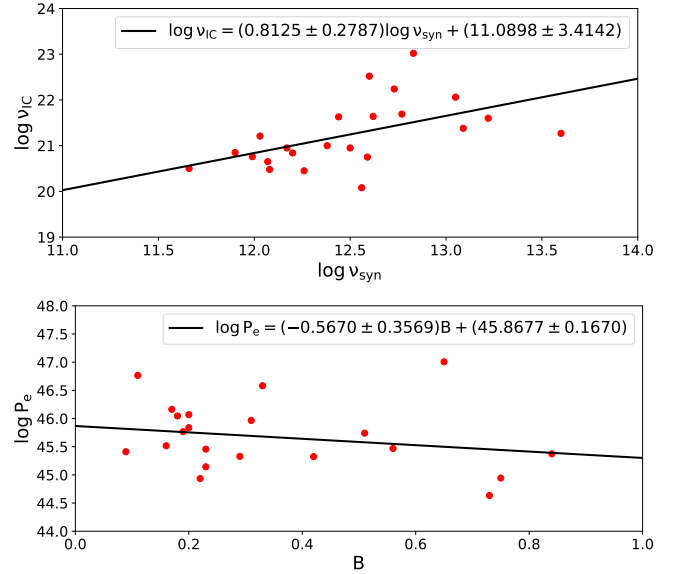


Figure 5. Linear relationships between the synchrotron peak frequency and IC peak frequency ($r = 0.5244$, $p = 0.0102$) and magnetic field and electron power ($r = -0.4903$, $p = 0.0175$) are shown.

tected. Among them, the object with the highest flux is B3 1343+451, and the lowest is PMN J0833-0454.

The synchrotron peak frequencies are in the range of $(0.46\text{--}39.81) \times 10^{12}$ Hz, which is typical for low-synchrotron-peaked blazars. The accretion disk luminosities are between $(0.69\text{--}10.96) \times 10^{46}$ erg s $^{-1}$, with an average value of 3.29×10^{46} erg s $^{-1}$; these values are characteristic of powerful blazars. We find that the jet powers are larger than their disk luminosities, which is consistent with result of Xiong & Zhang (2014); Ghisellini et al. (2010a). The BH masses in our sample are generally $> 10^{8.5} M_{\odot}$, because blazars with larger disk luminosities have larger BH masses (Ghisellini et al. 2010a; Potter & Cotter 2013). The disk luminosities of these sources do not exceed their Eddington luminosities, however, where the ratio $L_{\text{disk}}/L_{\text{Edd}} \sim 0.01\text{--}0.37$. This suggests that high-redshift blazars are likely in a sub-Eddington accretion state, where the typical standard thin disk, i.e., the Shakura–Sunyaev disk, can sufficiently explain their accretion structure (Shakura & Sunyaev 1973; Yuan & Narayan 2014; Xie et al. 2024).

We find that, in general, the closer the radiation region is to the central BH, the stronger its magnetic field. For high-redshift blazars, we find that the energy density of external photons from the MT—mainly IR photons from the MT—is approximately $(10^{-3}\text{--}10^{-2})$ erg cm $^{-3}$, while the energy density of the external photon field near the BLR—mainly UV photons from the BLR—is $(10^{-1}\text{--}10^0)$ erg cm $^{-3}$. This is related to the stronger

UV photon field in the BLR and the weaker IR photon field in the MT region. Additionally, these energy densities of high-redshift FSRQs are generally larger than their low-redshift counterparts (Zhang et al. 2024).

When the radiation region is near the MT, the EED spectral index is ~ 2 , consistent with shock acceleration theories. Near the BLR, the EED spectral index is typically > 4 , which is also within the expected range from standard particle acceleration theories (Achterberg et al. 2001; Ostrowski & Bednarz 2002; Keshet & Waxman 2005; Virtanen & Vainio 2005). Moreover, since the kinetic power in both radiation region positions is greater than the radiation power, the jets can exist stably, making it impossible to distinguish the radiation region position directly based solely on the fitted parameters. However, since the chi-square (χ^2) values obtained when the radiation region is near the MT are generally smaller, we infer that the radiation region may be near the MT, which is assumed in the subsequent analysis.

In the MT case, except for S4 1427+543, PKS 2311-452, PKS 0438-43, PKS 0834-20, and TXS 0222+185, the soft photons in the FSRQ γ -ray emission can be entirely explained by IR photons from the MT. The total jet power ranges from $(0.05\text{--}381.75) \times 10^{46} \text{ erg s}^{-1}$, with an average value of $4.47 \times 10^{47} \text{ erg s}^{-1}$, significantly larger than the jet power of low-redshift AGNs (Chen et al. 2023). Whether this result is due to selection effects or other factors, the high-redshift blazars considered here likely have larger kinetic and jet powers than their low-redshift counterparts. The disk luminosities and jet powers are nearly of the same order of magnitude, and the average ratio $\langle L_{\text{disk}}/L_{\text{jet}} \rangle \sim 2.93$, which is consistent with other studies (Rawlings & Saunders 1991; Maraschi & Tavecchio 2003; Ghisellini et al. 2010a; Luna-Cervantes et al. 2024), but differs from those obtained by Sahakyan et al. (2020); Xiong & Zhang (2014), possibly due to their omission of proton content in the jets.

4.2. Disk–Jet Connection Condition

By analyzing the average parameters and comparing them with their low-redshift counterparts, we can obtain the average properties of high-redshift blazars. Correlation analysis can further uncover the potential physical mechanisms. To explore the possible close connection between jets and accretion, we performed a correlation analysis on several parameters with a normal distribution.

There is a moderate negative correlation between the IC peak frequency (ν_{IC}) and the disk luminosity ($\log L_{\text{disk}}$), indicating that blazars with higher accretion disk luminosities tend to have lower IC peak frequencies,

possibly reflecting evolutionary effects or differences in the physical conditions of the radiation region (Ghisellini et al. 2011). High-luminosity accretion disks provide stronger external photon fields, leading to more efficient cooling of HE electrons, which reduces the IC peak frequency and increases the IC scattering flux (Fossati et al. 1998; Prandini & Ghisellini 2022).

The positive correlation between jet power (P_{jet}) and disk luminosity ($\log L_{\text{disk}}$), highlights the relationship between the accretion process and the jet launching mechanism, further supporting the accretion–jet connection theory (Maraschi & Tavecchio 2003; Volonteri et al. 2011; Ghisellini et al. 2013; Sharma et al. 2024), with disk luminosity possibly dominating over jet power (Ghisellini et al. 2014; Rajguru & Chatterjee 2022). Here, for high-redshift blazars, we have also found evidence supporting the accretion–jet connection.

Several well-established correlations further validate the validity of our results. First, a positive correlation between BH mass (M_{BH}) and disk luminosity (L_{disk}) is observed, as expected by Ghisellini et al. (2010a); Potter & Cotter (2013), since more massive BHs can accrete more material, leading to higher luminosities. Next, a positive correlation exists between the synchrotron peak frequency (ν_{syn}) and IC peak frequency (ν_{IC}). When ν_{syn} increases, corresponding to a larger Γ , IC-scattered photons are boosted to higher energies. This is also consistent with radiation models where emission at both peaks originates from the same population of electrons (Iyida et al. 2020). Third, the negative correlation between B' and $\log P_e$ arises because the magnetic field strength is related to synchrotron power. Stronger magnetic fields enhance synchrotron cooling, thereby affecting the EED and electron power.

Our analysis of high-redshift blazars provides valuable insights into the radiation properties of their jets, which exhibit higher γ -ray luminosities and softer spectral indices than their lower-redshift counterparts. By constructing and analyzing the average SEDs of a sample of high-redshift blazars ($z > 2.5$), we reduced the uncertainties caused by lower-quality data typical of individual high-redshift blazars.

In our analysis, we found that the majority of the γ -ray seed photons are likely IR photons from the MT, and hence the radiation region is more likely located near the MT. Compared to their low-redshift counterparts, high-redshift blazars exhibit higher γ -ray luminosities, jet power, kinetic power, energy densities, BH mass, and accretion disk luminosities.

All objects have an accretion disk luminosity lower than their Eddington luminosity, indicating sub-Eddington accretion. The accretion structure can be

explained by the Shakura–Sunyaev disk model. The EED spectral index is ~ 2 , and the electron acceleration mechanism is consistent with diffusive shock acceleration of nonrelativistic electrons. The $\nu_{\text{IC}}-L_{\text{disk}}$ correlation supports the idea that early AGNs have a higher external photon field density. The $P_{\text{jet}}-L_{\text{disk}}$ we observed correlation further supports the accretion–jet connection.

This work was partly supported by the National Science Foundation of China (grant nos. 12263007 and 12233006) and the High-level Talent Support Program of Yunnan Province.

APPENDIX

A. γ -RAY BAND SPECTRAL ENERGY DISTRIBUTIONS

In this appendix, the γ -ray band SEDs of the objects in our high-redshift blazar sample are presented.

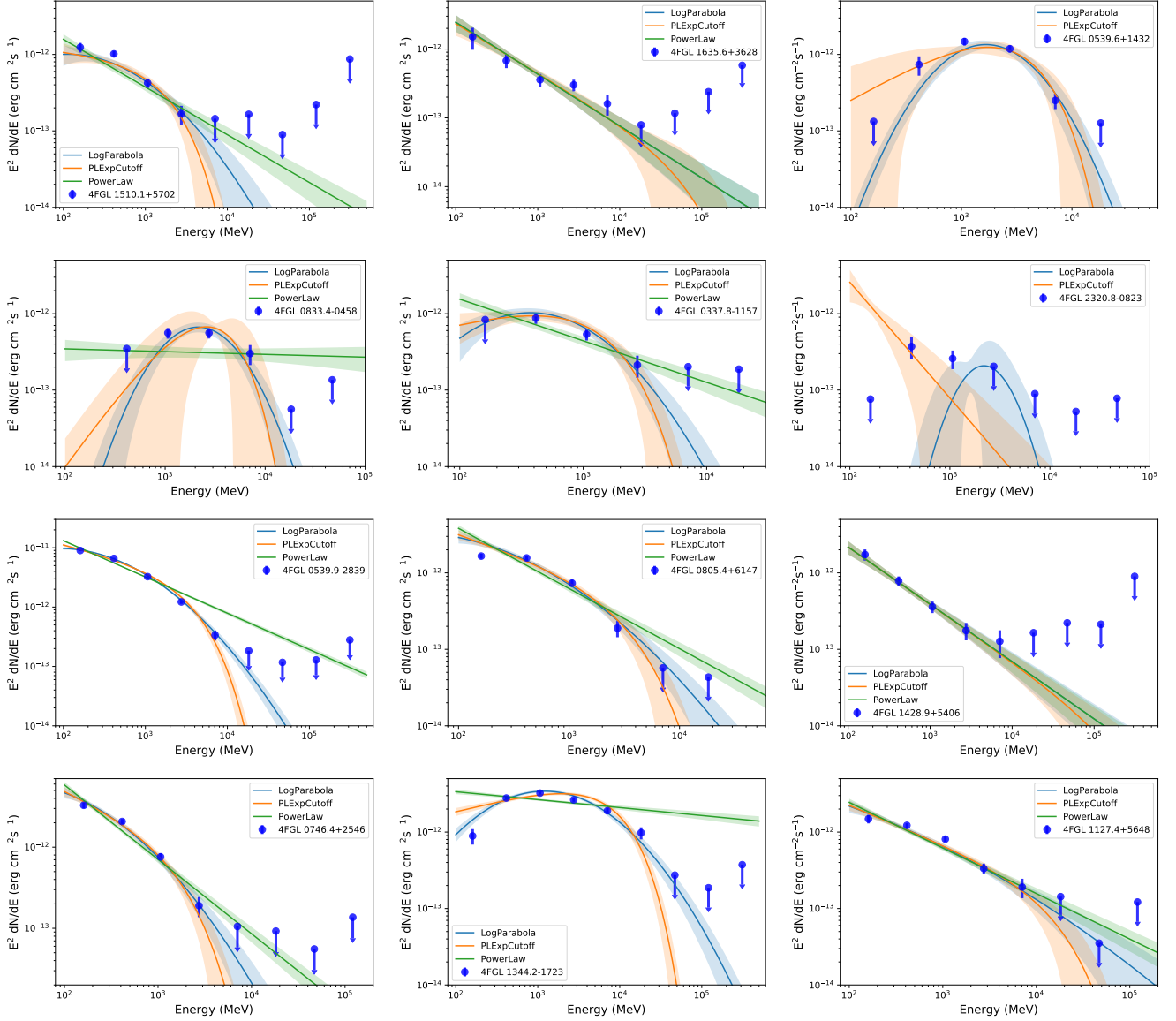


Figure 6. γ -ray spectra of high-redshift blazars. The symbols and lines are the same as shown in Figure 1.

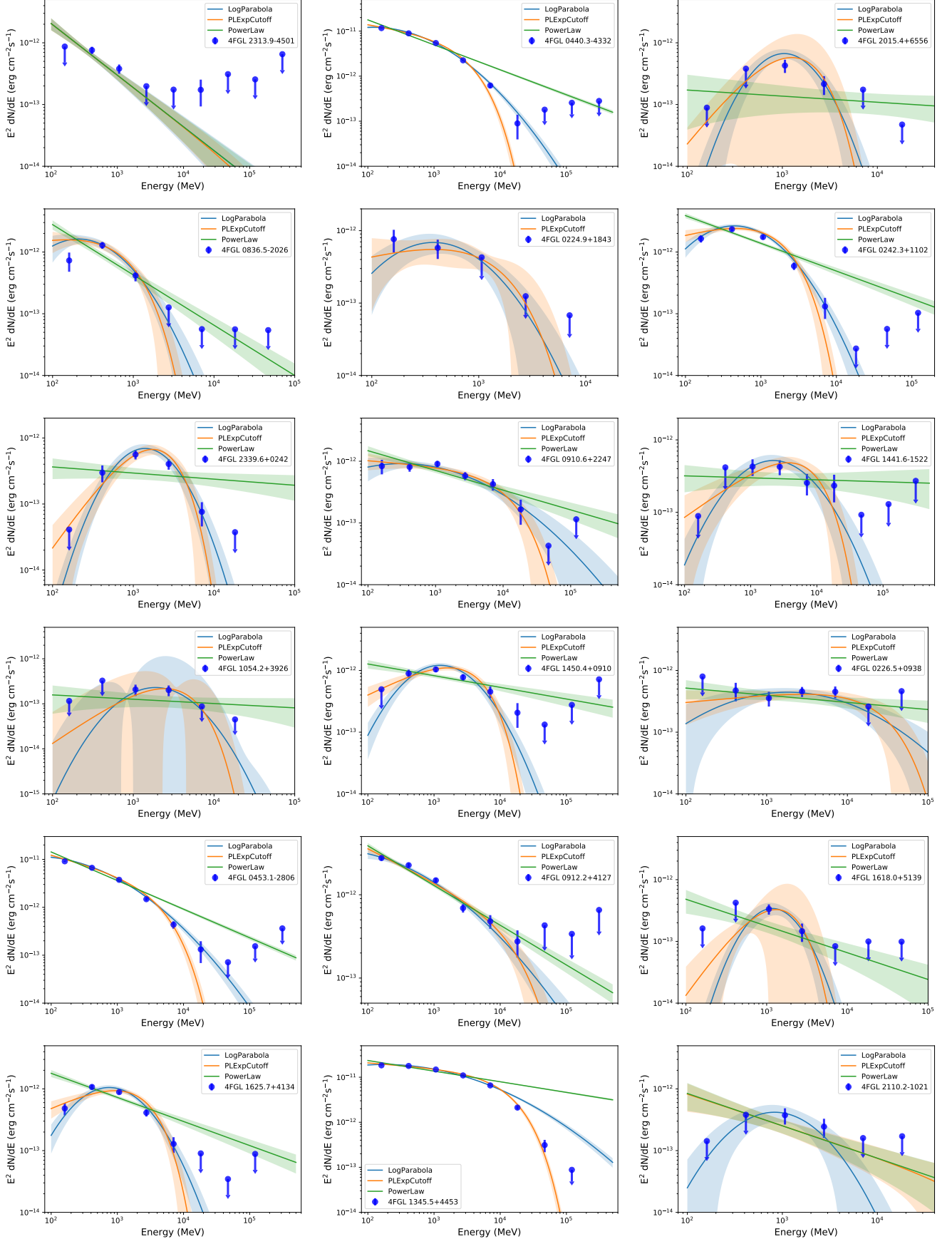


Figure 7. γ -ray spectra of high-redshift blazars. The symbols and lines are the same as shown in Figure 1.

B. MULTIWAVELENGTH SPECTRAL ENERGY DISTRIBUTION FITTING DIAGRAMS

In this appendix, the results of modelling the high-redshift blazars in terms of theoretical SEDs are presented.

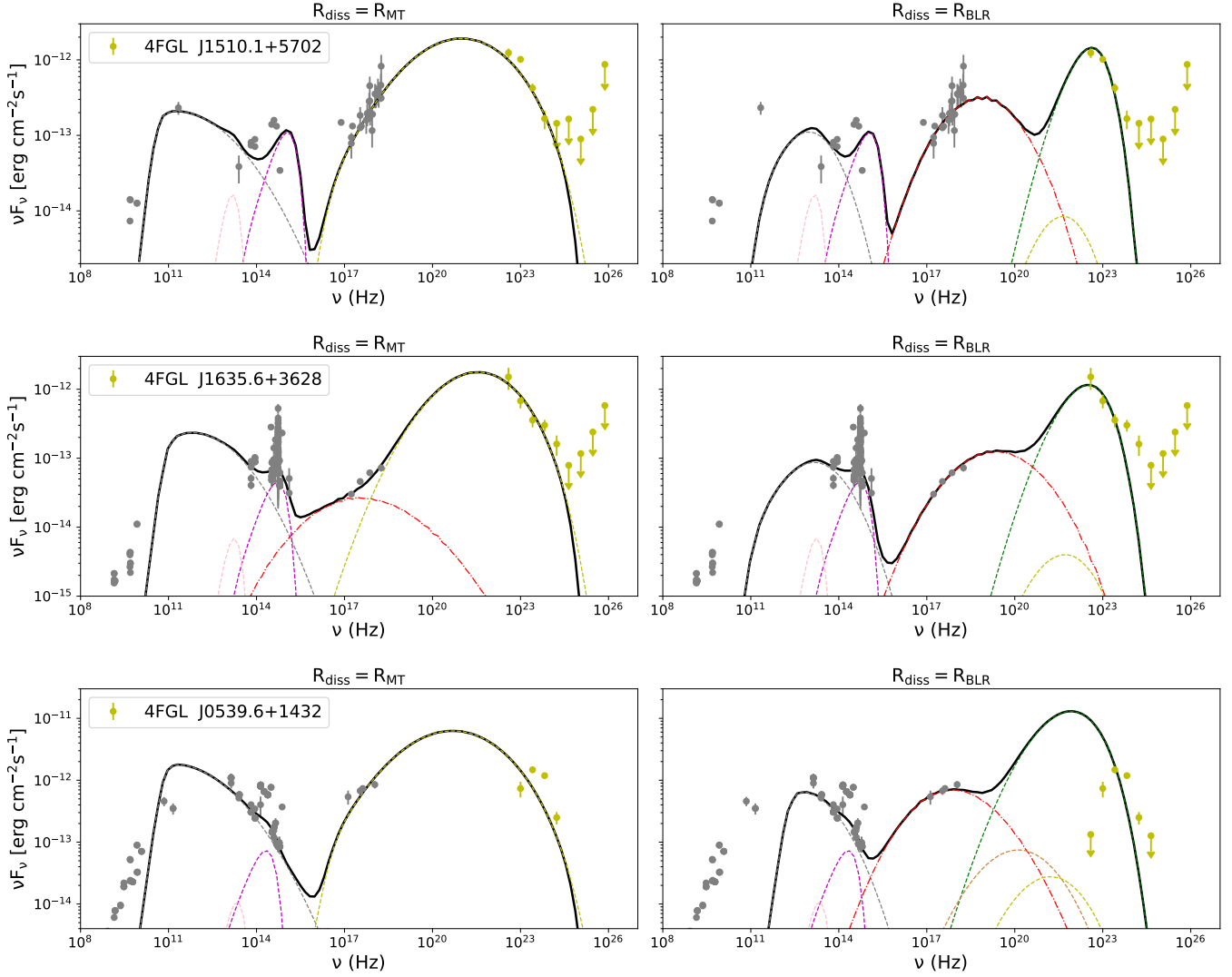


Figure 8. Theoretical modeling of the SEDs of 23 high-redshift blazars. The symbols and lines are the same as shown in Figure 2.

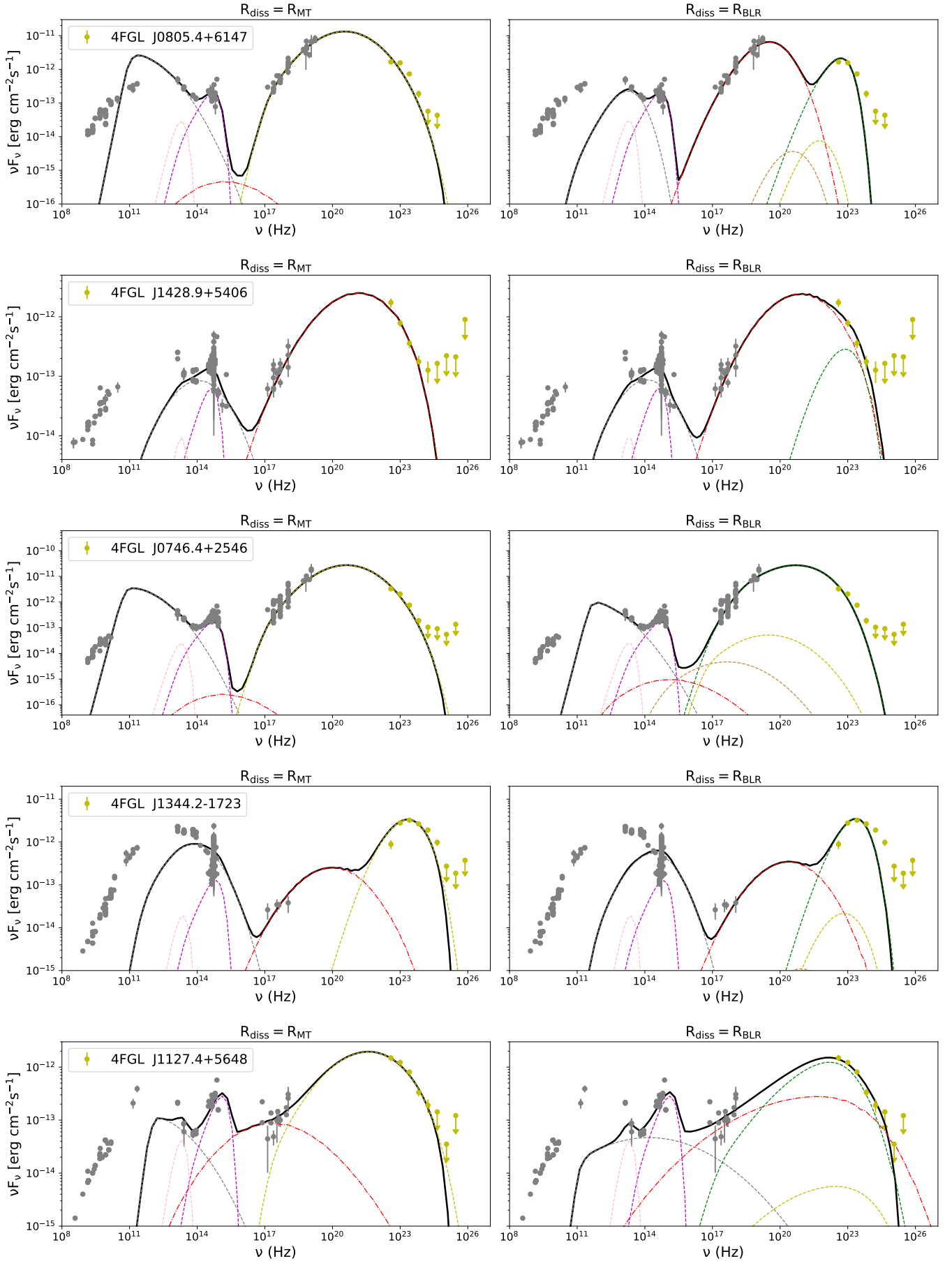


Figure 9. The symbols and lines are the same as shown in Figure 2.

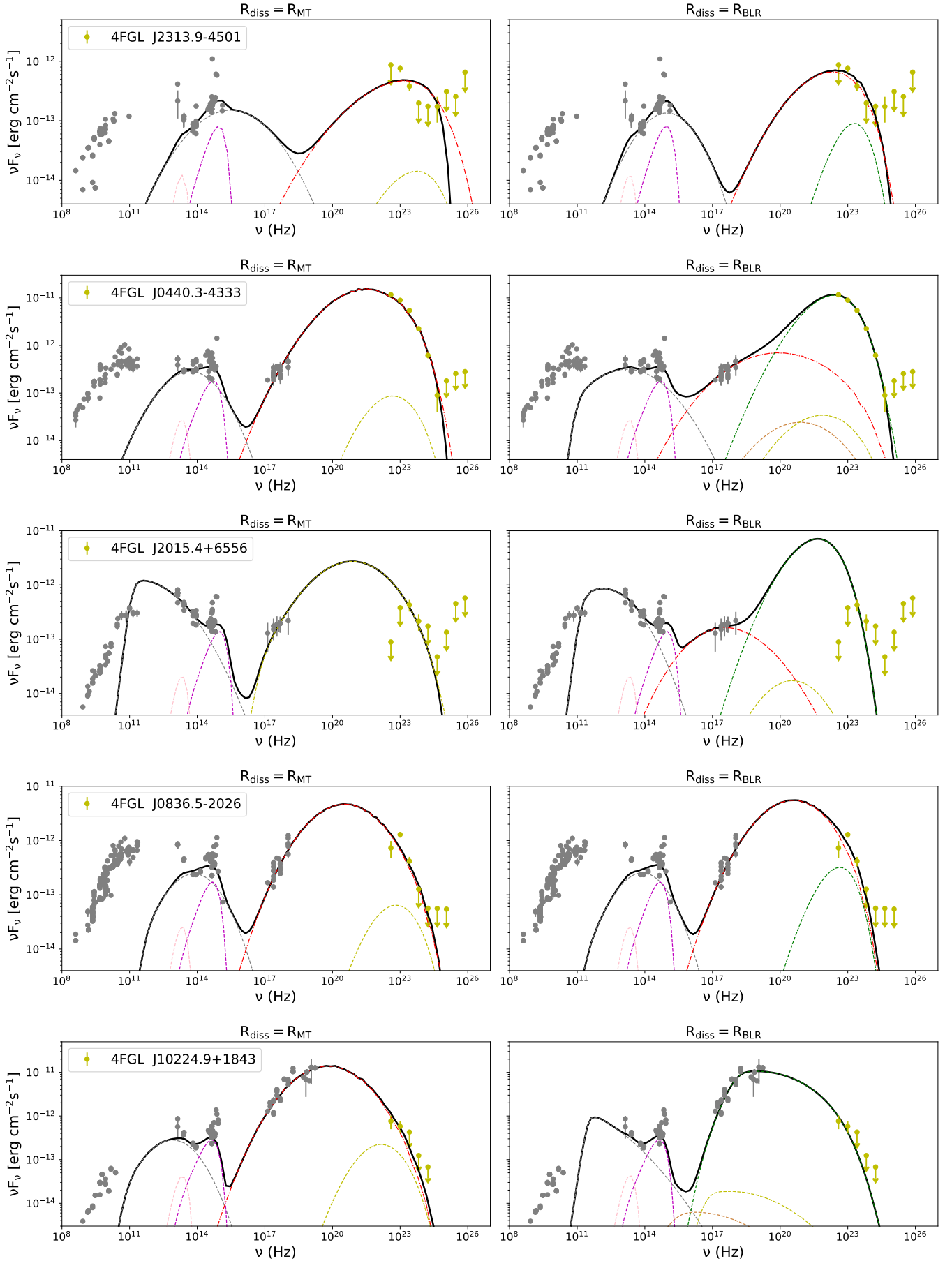


Figure 10. The symbols and lines are the same as shown in Figure 2.

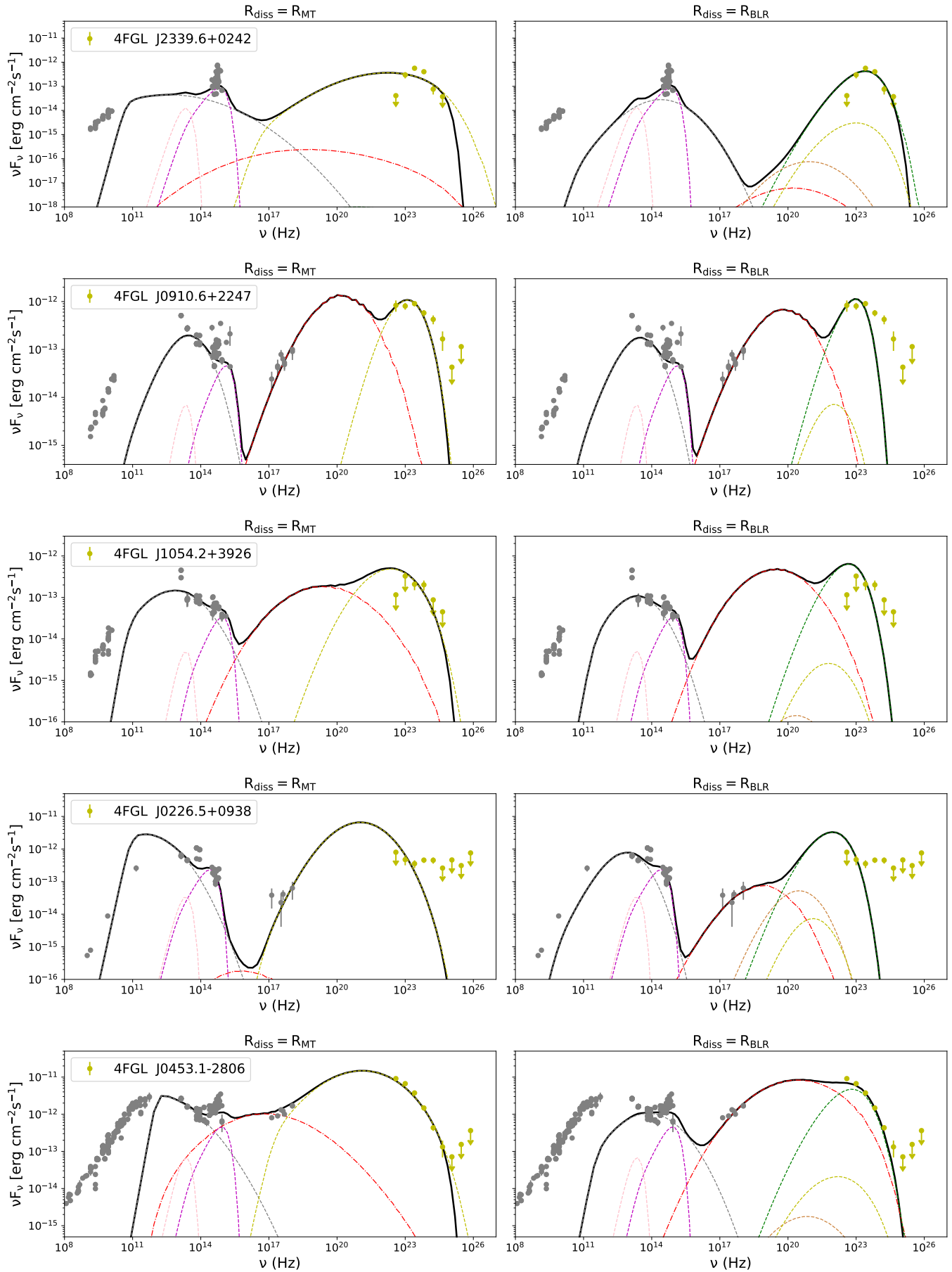


Figure 11. The symbols and lines are the same as shown in Figure 2.

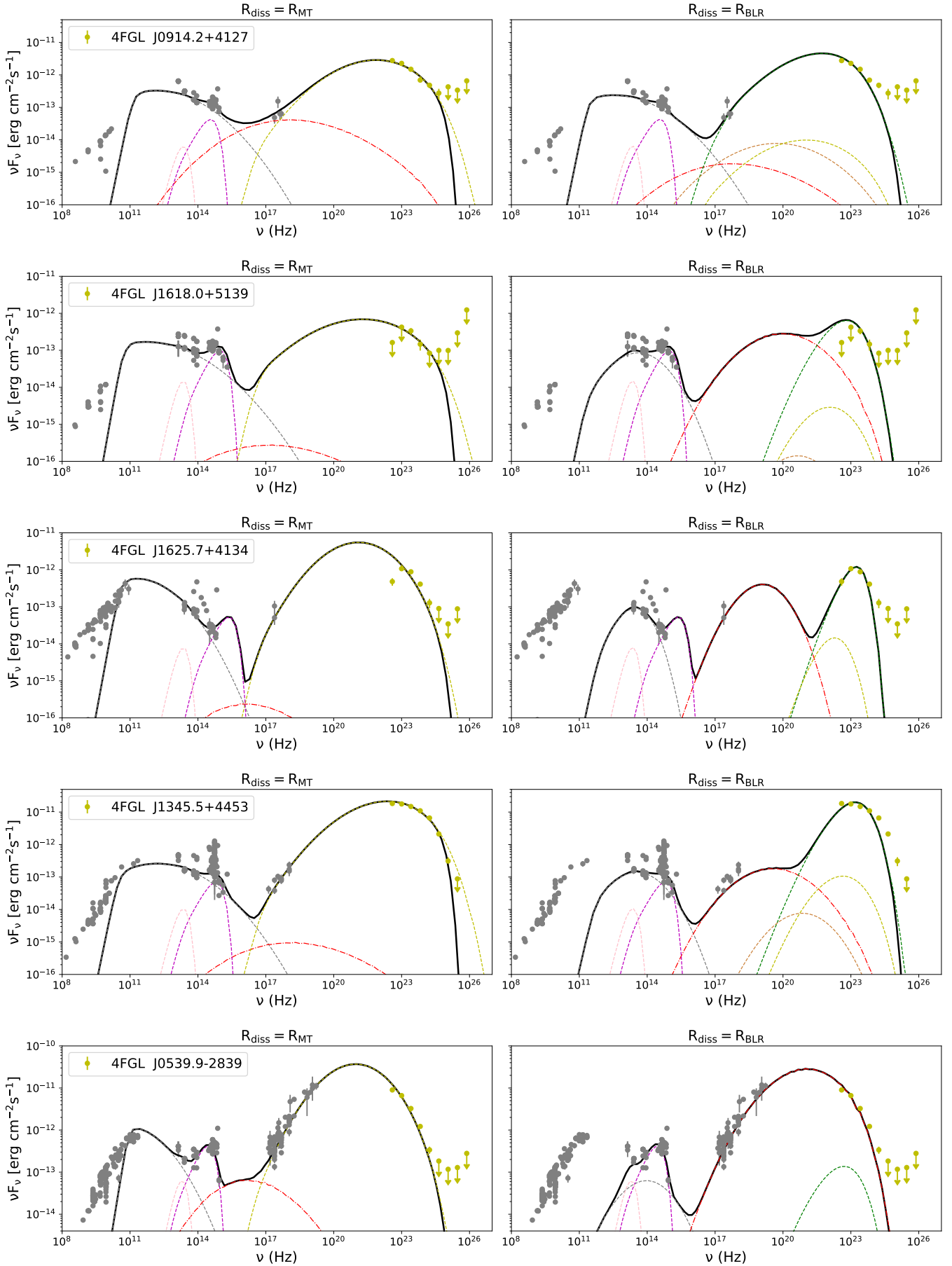


Figure 12. The symbols and lines are the same as shown in Figure 2.

REFERENCES

- Abdollahi, S., Acero, F., Ackermann, M., et al. 2020, *ApJS*, 247, 33, doi: [10.3847/1538-4365/ab6bcb](https://doi.org/10.3847/1538-4365/ab6bcb)
- Abdollahi, S., Acero, F., Baldini, L., et al. 2022, *ApJS*, 260, 53, doi: [10.3847/1538-4365/ac6751](https://doi.org/10.3847/1538-4365/ac6751)
- Achterberg, A., Gallant, Y. A., Kirk, J. G., & Guthmann, A. W. 2001, *MNRAS*, 328, 393, doi: [10.1046/j.1365-8711.2001.04851.x](https://doi.org/10.1046/j.1365-8711.2001.04851.x)
- Ackermann, M., Ajello, M., Allafort, A., et al. 2012, *Science*, 338, 1190, doi: [10.1126/science.1227160](https://doi.org/10.1126/science.1227160)
- Atwood, W. B., Abdo, A. A., Ackermann, M., et al. 2009, *ApJ*, 697, 1071, doi: [10.1088/0004-637X/697/2/1071](https://doi.org/10.1088/0004-637X/697/2/1071)
- Blażejowski, M., Sikora, M., Moderski, R., & Madejski, G. M. 2000, *ApJ*, 545, 107, doi: [10.1086/317791](https://doi.org/10.1086/317791)
- Bloom, S. D., & Marscher, A. P. 1996, *ApJ*, 461, 657, doi: [10.1086/177092](https://doi.org/10.1086/177092)
- Celotti, A., & Ghisellini, G. 2008, *MNRAS*, 385, 283, doi: [10.1111/j.1365-2966.2007.12758.x](https://doi.org/10.1111/j.1365-2966.2007.12758.x)
- Chen, Y., Gu, Q., Fan, J., et al. 2023, *ApJS*, 268, 6, doi: [10.3847/1538-4365/ace444](https://doi.org/10.3847/1538-4365/ace444)
- Chiang, C. Y., Done, C., Still, M., & Godet, O. 2010, *MNRAS*, 403, 1102, doi: [10.1111/j.1365-2966.2009.16129.x](https://doi.org/10.1111/j.1365-2966.2009.16129.x)
- Costamante, L., Cutini, S., Tosti, G., Antolini, E., & Tramacere, A. 2018, *MNRAS*, 477, 4749, doi: [10.1093/mnras/sty887](https://doi.org/10.1093/mnras/sty887)
- Dermer, C. D., & Schlickeiser, R. 2002, *ApJ*, 575, 667, doi: [10.1086/341431](https://doi.org/10.1086/341431)
- Desai, A., Helgason, K., Ajello, M., et al. 2019, *ApJL*, 874, L7, doi: [10.3847/2041-8213/ab0c10](https://doi.org/10.3847/2041-8213/ab0c10)
- Fan, J., Xiao, H., Yang, W., et al. 2023, *ApJS*, 268, 23, doi: [10.3847/1538-4365/ace7c8](https://doi.org/10.3847/1538-4365/ace7c8)
- Fermi-LAT Collaboration, Abdollahi, S., Ackermann, M., et al. 2018, *Science*, 362, 1031, doi: [10.1126/science.aat8123](https://doi.org/10.1126/science.aat8123)
- Finke, J. D., Ajello, M., Domínguez, A., et al. 2022, *ApJ*, 941, 33, doi: [10.3847/1538-4357/ac9843](https://doi.org/10.3847/1538-4357/ac9843)
- Finke, J. D., Razzaque, S., & Dermer, C. D. 2010, *ApJ*, 712, 238, doi: [10.1088/0004-637X/712/1/238](https://doi.org/10.1088/0004-637X/712/1/238)
- Foreman-Mackey, D., Hogg, D. W., Lang, D., & Goodman, J. 2013, *PASP*, 125, 306, doi: [10.1086/670067](https://doi.org/10.1086/670067)
- Fossati, G., Maraschi, L., Celotti, A., Comastri, A., & Ghisellini, G. 1998, *MNRAS*, 299, 433, doi: [10.1046/j.1365-8711.1998.01828.x](https://doi.org/10.1046/j.1365-8711.1998.01828.x)
- Franceschini, A., Rodighiero, G., & Vaccari, M. 2008, *A&A*, 487, 837, doi: [10.1051/0004-6361:200809691](https://doi.org/10.1051/0004-6361:200809691)
- Ghisellini, G., George, I. M., & Done, C. 1989, *MNRAS*, 241, 43P, doi: [10.1093/mnras/241.1.43P](https://doi.org/10.1093/mnras/241.1.43P)
- Ghisellini, G., Haardt, F., Della Ceca, R., Volonteri, M., & Sbarrato, T. 2013, *MNRAS*, 432, 2818, doi: [10.1093/mnras/stt637](https://doi.org/10.1093/mnras/stt637)
- Ghisellini, G., Maraschi, L., & Treves, A. 1985, *A&A*, 146, 204
- Ghisellini, G., & Tavecchio, F. 2008, *MNRAS*, 387, 1669, doi: [10.1111/j.1365-2966.2008.13360.x](https://doi.org/10.1111/j.1365-2966.2008.13360.x)
- . 2009, *MNRAS*, 397, 985, doi: [10.1111/j.1365-2966.2009.15007.x](https://doi.org/10.1111/j.1365-2966.2009.15007.x)
- Ghisellini, G., Tavecchio, F., Foschini, L., et al. 2010a, *MNRAS*, 402, 497, doi: [10.1111/j.1365-2966.2009.15898.x](https://doi.org/10.1111/j.1365-2966.2009.15898.x)
- Ghisellini, G., Tavecchio, F., Maraschi, L., Celotti, A., & Sbarrato, T. 2014, *Nature*, 515, 376, doi: [10.1038/nature13856](https://doi.org/10.1038/nature13856)
- Ghisellini, G., Della Ceca, R., Volonteri, M., et al. 2010b, *MNRAS*, 405, 387, doi: [10.1111/j.1365-2966.2010.16449.x](https://doi.org/10.1111/j.1365-2966.2010.16449.x)
- Ghisellini, G., Tagliaferri, G., Foschini, L., et al. 2011, *MNRAS*, 411, 901, doi: [10.1111/j.1365-2966.2010.17723.x](https://doi.org/10.1111/j.1365-2966.2010.17723.x)
- Iyida, E. U., Odo, F. C., Chukwude, A. E., & Ubachukwu, A. A. 2020, *Open Astronomy*, 29, 168, doi: [10.1515/astro-2020-0015](https://doi.org/10.1515/astro-2020-0015)
- Jones, F. C. 1968, *Physical Review*, 167, 1159, doi: [10.1103/PhysRev.167.1159](https://doi.org/10.1103/PhysRev.167.1159)
- Keshet, U., & Waxman, E. 2005, *PhRvL*, 94, 111102, doi: [10.1103/PhysRevLett.94.111102](https://doi.org/10.1103/PhysRevLett.94.111102)
- Landau, R., Golisch, B., Jones, T. J., et al. 1986, *ApJ*, 308, 78, doi: [10.1086/164480](https://doi.org/10.1086/164480)
- Luna-Cervantes, J., Tramacere, A., & Benítez, E. 2024, *MNRAS*, 532, 3729, doi: [10.1093/mnras/stae1687](https://doi.org/10.1093/mnras/stae1687)
- Maraschi, L., & Tavecchio, F. 2003, *ApJ*, 593, 667, doi: [10.1086/342118](https://doi.org/10.1086/342118)
- Marcotulli, L., Paliya, V., Ajello, M., et al. 2020, *ApJ*, 889, 164, doi: [10.3847/1538-4357/ab65f5](https://doi.org/10.3847/1538-4357/ab65f5)
- Massaro, E., Tramacere, A., Perri, M., Giommi, P., & Tosti, G. 2006, *A&A*, 448, 861, doi: [10.1051/0004-6361:20053644](https://doi.org/10.1051/0004-6361:20053644)
- Narayan, R., & Raymond, J. 1999, *ApJL*, 515, L69, doi: [10.1086/311973](https://doi.org/10.1086/311973)
- Narayan, R., Sądowski, A., & Soria, R. 2017, *MNRAS*, 469, 2997, doi: [10.1093/mnras/stx1027](https://doi.org/10.1093/mnras/stx1027)
- Nolan, P. L., Abdo, A. A., Ackermann, M., et al. 2012, *ApJS*, 199, 31, doi: [10.1088/0067-0049/199/2/31](https://doi.org/10.1088/0067-0049/199/2/31)
- Ostrowski, M., & Bednarz, J. 2002, *A&A*, 394, 1141, doi: [10.1051/0004-6361:20021173](https://doi.org/10.1051/0004-6361:20021173)
- Paliya, V. S., Ajello, M., Cao, H. M., et al. 2020, *ApJ*, 897, 177, doi: [10.3847/1538-4357/ab9c1a](https://doi.org/10.3847/1538-4357/ab9c1a)
- Paliya, V. S., Domínguez, A., Ajello, M., Olmo-García, A., & Hartmann, D. 2021, *ApJS*, 253, 46, doi: [10.3847/1538-4365/abe135](https://doi.org/10.3847/1538-4365/abe135)

- Paliya, V. S., Marcotulli, L., Ajello, M., et al. 2017, *ApJ*, 851, 33, doi: [10.3847/1538-4357/aa98e1](https://doi.org/10.3847/1538-4357/aa98e1)
- Potter, W. J., & Cotter, G. 2013, *MNRAS*, 431, 1840, doi: [10.1093/mnras/stt300](https://doi.org/10.1093/mnras/stt300)
- Prandini, E., & Ghisellini, G. 2022, *Galaxies*, 10, 35, doi: [10.3390/galaxies10010035](https://doi.org/10.3390/galaxies10010035)
- Rajguru, G., & Chatterjee, R. 2022, *PhRvD*, 106, 063001, doi: [10.1103/PhysRevD.106.063001](https://doi.org/10.1103/PhysRevD.106.063001)
- Rawlings, S., & Saunders, R. 1991, *Nature*, 349, 138, doi: [10.1038/349138a0](https://doi.org/10.1038/349138a0)
- Rees, M. J., Begelman, M. C., Blandford, R. D., & Phinney, E. S. 1982, *Nature*, 295, 17, doi: [10.1038/295017a0](https://doi.org/10.1038/295017a0)
- Sahakyan, N. 2020, *MNRAS*, 496, 5518, doi: [10.1093/mnras/staa1893](https://doi.org/10.1093/mnras/staa1893)
- Sahakyan, N., Israyelyan, D., Harutyunyan, G., Khachatryan, M., & Gasparyan, S. 2020, *MNRAS*, 498, 2594, doi: [10.1093/mnras/staa2477](https://doi.org/10.1093/mnras/staa2477)
- Shakura, N. I., & Sunyaev, R. A. 1973, *A&A*, 24, 337
- Sharma, A., Kamaram, S. R., Prince, R., Khatoon, R., & Bose, D. 2024, *MNRAS*, 527, 2672, doi: [10.1093/mnras/stad3399](https://doi.org/10.1093/mnras/stad3399)
- Sikora, M., Begelman, M. C., & Rees, M. J. 1994, *ApJ*, 421, 153, doi: [10.1086/173633](https://doi.org/10.1086/173633)
- Sikora, M., Stawarz, L., Moderski, R., Nalewajko, K., & Madejski, G. M. 2009, *ApJ*, 704, 38, doi: [10.1088/0004-637X/704/1/38](https://doi.org/10.1088/0004-637X/704/1/38)
- Stecker, F. W., Baring, M. G., & Summerlin, E. J. 2007, *ApJL*, 667, L29, doi: [10.1086/522005](https://doi.org/10.1086/522005)
- Stickel, M., Padovani, P., Urry, C. M., Fried, J. W., & Kuehr, H. 1991, *ApJ*, 374, 431, doi: [10.1086/170133](https://doi.org/10.1086/170133)
- Sulentic, J. W., Marziani, P., & Dultzin-Hacyan, D. 2000, *ARA&A*, 38, 521, doi: [10.1146/annurev.astro.38.1.521](https://doi.org/10.1146/annurev.astro.38.1.521)
- Taam, R. E., Liu, B. F., Yuan, W., & Qiao, E. 2012, *ApJ*, 759, 65, doi: [10.1088/0004-637X/759/1/65](https://doi.org/10.1088/0004-637X/759/1/65)
- Thorne, K. S. 1974, *ApJ*, 191, 507, doi: [10.1086/152991](https://doi.org/10.1086/152991)
- Tramacere, A., Giommi, P., Perri, M., Verrecchia, F., & Tosti, G. 2009, *A&A*, 501, 879, doi: [10.1051/0004-6361/200810865](https://doi.org/10.1051/0004-6361/200810865)
- Tramacere, A., Massaro, E., & Taylor, A. M. 2011, *ApJ*, 739, 66, doi: [10.1088/0004-637X/739/2/66](https://doi.org/10.1088/0004-637X/739/2/66)
- Urry, C. M., & Padovani, P. 1995, *PASP*, 107, 803, doi: [10.1086/133630](https://doi.org/10.1086/133630)
- Virtanen, J. J. P., & Vainio, R. 2005, *ApJ*, 621, 313, doi: [10.1086/427324](https://doi.org/10.1086/427324)
- Volonteri, M., Haardt, F., Ghisellini, G., & Della Ceca, R. 2011, *MNRAS*, 416, 216, doi: [10.1111/j.1365-2966.2011.19024.x](https://doi.org/10.1111/j.1365-2966.2011.19024.x)
- Wielgus, M., Lančová, D., Straub, O., et al. 2022, *MNRAS*, 514, 780, doi: [10.1093/mnras/stac1317](https://doi.org/10.1093/mnras/stac1317)
- Wu, F., Hu, W., & Dai, B. 2024, *ApJ*, 972, 183, doi: [10.3847/1538-4357/ad5f8a](https://doi.org/10.3847/1538-4357/ad5f8a)
- Xiao, H., Ouyang, Z., Zhang, L., et al. 2022, *ApJ*, 925, 40, doi: [10.3847/1538-4357/ac36da](https://doi.org/10.3847/1538-4357/ac36da)
- Xie, S., Ouyang, Z., Wu, J., et al. 2024, *ApJ*, 976, 78, doi: [10.3847/1538-4357/ad8353](https://doi.org/10.3847/1538-4357/ad8353)
- Xiong, D. R., & Zhang, X. 2014, *MNRAS*, 441, 3375, doi: [10.1093/mnras/stu755](https://doi.org/10.1093/mnras/stu755)
- Yuan, F., & Narayan, R. 2004, *ApJ*, 612, 724, doi: [10.1086/422802](https://doi.org/10.1086/422802)
- . 2014, *ARA&A*, 52, 529, doi: [10.1146/annurev-astro-082812-141003](https://doi.org/10.1146/annurev-astro-082812-141003)
- Zhang, L., Chen, X., He, S., et al. 2024, *ApJS*, 271, 27, doi: [10.3847/1538-4365/ad20c8](https://doi.org/10.3847/1538-4365/ad20c8)
- Zhu, K. R., Chen, J. M., & Zhang, L. 2024, *ApJS*, 275, 41, doi: [10.3847/1538-4365/ad8639](https://doi.org/10.3847/1538-4365/ad8639)